Technical University of Denmark

DTU

KNOW-BLADE task-3.3 report: Rotor blade computations with 3D vortex generators

Johansen, Jeppe; Sørensen, Niels N.; Reck, M.; Hansen, M.O.L.; Stuermer, A.; Ramboer, J.; Hirsch, C.; Ekaterinaris, J.; Voutsinas, S.; Perivolaris, Y.

Publication date:
2005

Document Version
Publisher's PDF, also known as Version of record

Link back to DTU Orbit

DTU Library
Technical Information Center of Denmark

KNOW-BLADE Task-3.3 report; Rotor Blade Computations with 3D Vortex Generators

Jeppe Johansen, Niels N. Sørensen, Mads Reck, Martin O.L.Hansen, Arne Stuermer, Jan Ramboer, Charles Hirsch,John Ekaterinaris, Spyros Voutsinas and Yannis Perivolaris

Author: Jeppe Johansen, Niels N. Sørensen, Mads Reck, Martin O.L.Hansen, Arne Stuermer, Jan Ramboer, Charles Hirsch,John Ekaterinaris, Spyros Voutsinas and Yannis Perivolaris
Title: KNOW-BLADE Task-3.3 report; Rotor Blade Computations with 3D Vortex Generators

Abstract (max. 2000 char.):
The present report describes the work done in work package WP3.3: Aerodynamic Accessories in 3D in the EC project KNOW-BLADE. Vortex generators (VGs) are modelled in 3D Navier-Stokes solvers and applied on the flow around an airfoil and a wind turbine blade. Three test cases have been investigated. They are:

- A non-rotating airfoil section with VGs
- A rotating airfoil section with VGs
- A non-rotating wind turbine blade with VGs

The airfoil section was the FFA-W3-241 airfoil, which has been measured in the VELUX wind tunnel with and without VGs placed at different chordwise positions. Three of the partners have modelled the airfoil section as a thin airfoil section with symmetry boundary conditions in the spanwise direction to simulate an array of VGs.
The wind turbine blade is the LM19.1 blade equipped with one pair of VGs placed at radius = 8.5 m.

In general all partners have successfully modelled vortex generators in 3D, which eventually generates vortices and mixes the boundary layer. A large effort has been on generating the numerical meshes since this is a relatively complex configuration and a large variation of length and time scales is present. Even though the quantitative agreement with measurements is not acceptable the effort spend in the present project indicate that it is possible to investigate the effect of vortex generators on wind turbine blades using 3D Navier-Stokes solvers. Much further work within independence of mesh resolution and time step as well as turbulence modelling has to be carried out in future projects before parametric variations can be investigated.

Contents

Preface

The present work is made during the KNOW-BLADE EC project (contract number: ENK6-CT-2001-00503) in which nine partners are involved. These are:

Risø National Laboratory, Roskilde Denmark,	RISOE (Coordinator)
Centre for Renewable Energy Sources, Greece,	CRES
Deutches Zentrum fuer Luft- und Raumfahrt, Germany	DLR
Danmarks Tekniske Universitet, Denmark	DTU
Swedish Defence Research Agency, Sweden,	FOI
National Technical University of Athens, Greece	NTUA
Vrije Universiteit Brussels, Belgium	VUB
Foundation of Research and Technology, Greece	FORTH
LM Glasfiber A/S, Denmark	LMG

The main objective of the project is through research activities to fill in important knowledge gaps in the wind turbine community by applying Navier-Stokes (NS) solvers to a series of unsolved aerodynamic and aeroelastic problems. The present report describes the work carried out in work package WP3.3: Aerodynamic accessories in 3D in which DLR, NTUA, VUB, and FORTH are involved.

In connection with modern wind turbines a series of different aerodynamic accessories or devices are used for adjusting the aerodynamic and aeroelastic behaviour of wind turbine blades. Typical applications are to adjust the power or the loads of the turbine, or to prevent undesired vibrations or multileveled power curves. Several devices are frequently applied; of these the most widely used are stall-strips, vortex generators and trip-tape/zig-zag tape. The present report describes the modelling of vortex generators in 3D using different 3D Navier-Stokes codes and different numerical approaches.

As described in ref.[1] vortex generators are currently used to control the aerodynamic forces and increase the performance and predictability of some wind turbine rotors during operation. Finding the optimal chordwise position and spanwise spacing for vortex generators demands a lot of experimental investigations, which are expensive. The motivation for the present work is to investigate the possibilities of physically model the vortex generator in 3D and to compute the detailed effect of the generated vortices.

The delta wing shaped vortex generators are usually placed in an array of pairs on the suction side of the blade. See Figure 1.
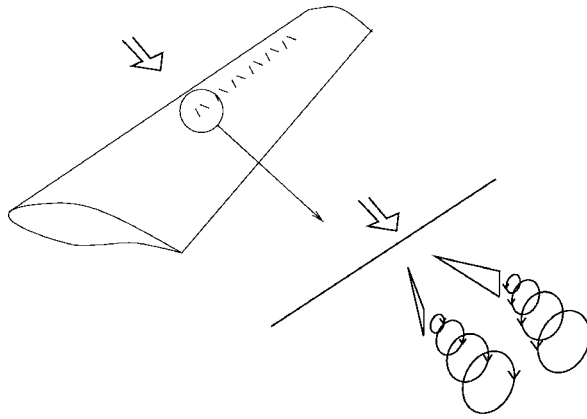
Figure 1: Schematic drawing showing the increased mixing due to vortex generators

When the flow passes the blade the vortex generators create a pair of contra-rotating vortices, which transport momentum from the upper part of the boundary layer to the lower part of the boundary layer, and thereby increases the mixing closer to the wall. This leads to a fuller streamwise velocity profile and causes the boundary layer to better withstand the adverse pressure gradient and thereby delaying separation.

Section 1 deals with the modelling of 3D vortex generators on a 3D airfoil section in uniform flow. Section 2 describes the flow around a rotating airfoil section equipped with vortex generators. Section 3 investigates the flow around a wind turbine blade in uniform flow equipped with one pair of vortex generators.

Each of the sections includes a short introduction followed by contributions of each of the individual partners. Finally, a discussion and conclusions of the results are drawn in Section 4.

Non-rotating 3D airfoil section with vortex generators

The test case chosen is the flow around the FFA-W3-241 airfoil section with and without vortex generators. A test case definition was decided upon and is described in Table 1, which corresponds to measurements performed by RISOE and described in .

Table 1: Test cases for the non-rotating airfoil section with and without vortex generators, Re 1.6·10[6].

Test cases	DLR	DTU	FORTH	NTUA
Smooth airfoil	8°, 14°, 18°	14°	8°, 14°, 18°	10.2°, 16°
4 mm VG placed at x/c=0.1	8°, 14°, 18°	14°	8°, 14°, 18°	
6 mm VG placed at x/c=0.1				14.4°
6 mm VG placed at x/c=0.2				5°, 10.2°, 12°, 14.4°, 16°, 19°
6 mm VG placed at x/c=0.3				14.4°

(The 4 and 6 mm VG corresponds to the height of the vortex generators used in the measurements, where the chord was 600 mm. I.e. 4mm ~ h/chord = $6.667 \cdot 10^{-3}$ and 6mm ~ h/chord = $1.0 \cdot 10^{-2}$)

Four partners are involved in the work. They are DLR, DTU, FORTH and NTUA. Measurements of both smooth and airfoil equipped with vortex generators are described in[2].

1.1 DLR contribution

In WP3.3 of the KNOWBLADE project, DLR performed a series of CFD simulations of the FFA-W3-241 airfoil aimed at numerically investigating the aerodynamic effects of vortex generators. The computations were done with the unstructured DLR TAU code. A complete 3D vortex generator was modelled with a novel use of symmetry boundary conditions and a grid refinement approach was employed to properly track the vortex.

Geometry and Test Case

Of the various configurations investigated by RISOE in a wind tunnel test campaign [2] two were selected for the DLR computations. The first is the clean FFA-W3-241 airfoil and the second is the same airfoil with a 4mm high vortex generator (VG) pair located at a chordwise position of x/c=0.1.

The geometric modelling of the vortex generator makes use of the parametric functionalities of the DLR-MegaCads tool [3]. The VG geometry is modelled as a volume with a thickness of less than 5% of its length at its base but with sharp edges. The reason this approach was taken is that the unstructured mesh generator used does not allow for zero thickness surfaces. In the experiment the tips of the leading edges of the two VGs of a pair were spaced 8 mm apart and the distance to the next pair was 20 mm, as described

in ref.. This symmetry and periodicity in the VG spacings allows the computational domain to be limited to a narrow spanwise section, with symmetry boundary conditions at a distance of 4 mm or 10 mm to the tip of the leading edge of the VG respectively. This geometric setup and the surface grid in the vicinity of the VG are shown in Figure 2.
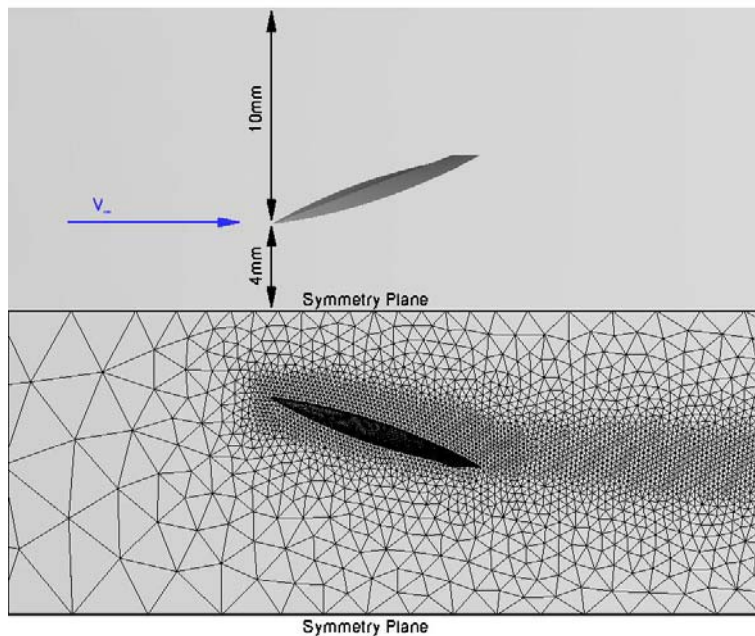

Figure 2: Geometric setup and surface grid

The meshes were generated using the CentaurSoft Centaur mesh generation package [4]. For both cases the boundary layer regions were resolved with 30 layers of prismatic cells, while tetrahedral elements are used for the rest of the computational domain. Centaur enables the specification of regions with a higher grid density. Due to the close proximity of the VGs vortex to the surface of the airfoil this feature was exploited in an attempt to improve vortex resolution. In an iterative approach alternating between grid generation and CFD computation, the grid was regenerated with appropriate refinement in several steps based on the track of the vortex seen in the CFD results.

For both configurations computations were run at the three angles of attack of 8°, 14° and 18° and at a Reynolds number of Re=$1.6 \cdot 10^6$ with fully turbulent flow, i.e. no laminar regions or transition specified.

Flow Solver

The computations were performed using the DLR TAU-code, which was developed in the MEGAFLOW project [5]. TAU is a 3D unstructured finite-volume CFD software package for the numerical simulation of a wide range of aerodynamic flows using the compressible Euler or the Reynolds-averaged Navier-Stokes equations. It utilizes an edge based data structure, also referred to as a dual grid approach, which serves to improve the memory efficiency of the solver and allows arbitrarily shaped mesh elements to be used. Various schemes are available for the discretization of the convective terms, with a central differencing scheme coupled with scalar dissipation chosen for the computations performed here. The viscous fluxes are discretized with a

central scheme. For these steady state computations an explicit 3-stage Runge-Kutta scheme is employed for the temporal integration of the governing equations and residual smoothing, local time-stepping and multigrid techniques help to accelerate convergence. Among the turbulence models implemented in TAU are the one-equation Spalart-Allmaras [6] and the two-equation Menter-SST model [7], which was selected for the work performed here after a series of numerical experiments. Furthermore, the DLR-TAU code offers solution based grid adaptation, which enables a proper resolution of the boundary layers to be achieved through an adjustment of cell spacing close to the surface as well as the addition or redistribution of grid nodes as required to improve the resolution of important aerodynamic flow features. Due to the use of the manual vortex tracking technique during the grid generation process described previously, the latter feature was not used here. However, the grid adaptation was employed once for each configuration at each angle of attack to adjust the wall normal spacing to ensure a y+ value of 1 was achieved on the surfaces of the airfoil.

Results

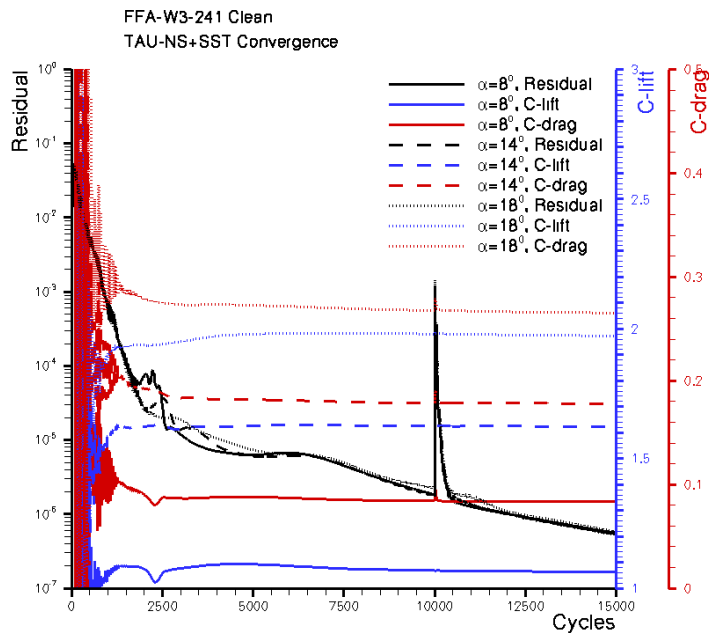Figure 3 shows the convergence of the computations of the clean airfoil cases.

Figure 3: Convergence of the clean airfoil computations.

The spike in the residual at 10000 cycles is due to the y+-based grid adaptation for proper boundary layer resolution. Figure 4 shows a comparison of the clean airfoil pressure distributions at the three angles of attack.
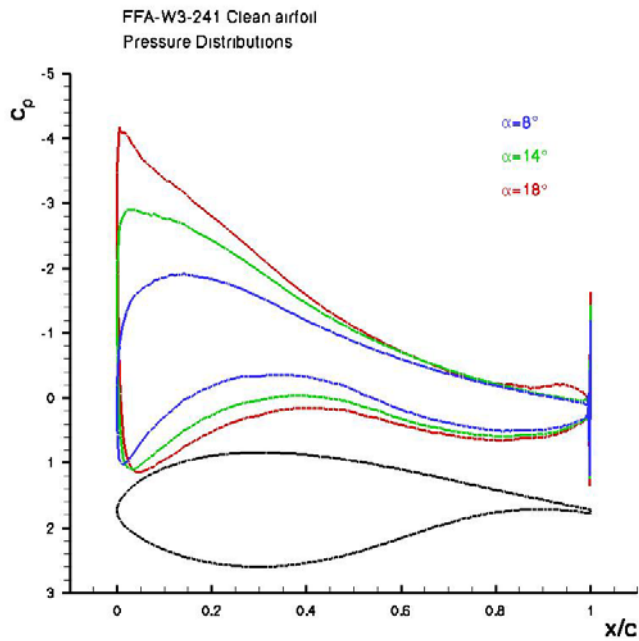
Figure 4: Pressure distribution for the clean airfoil.

The strong decrease in suction peak pressure levels with increasing angle of attack is clearly visible as is the development of a trailing edge separation region for the highest angle of attack of 18°. This separation region is also visible in the streamlines shown in Figure 5.
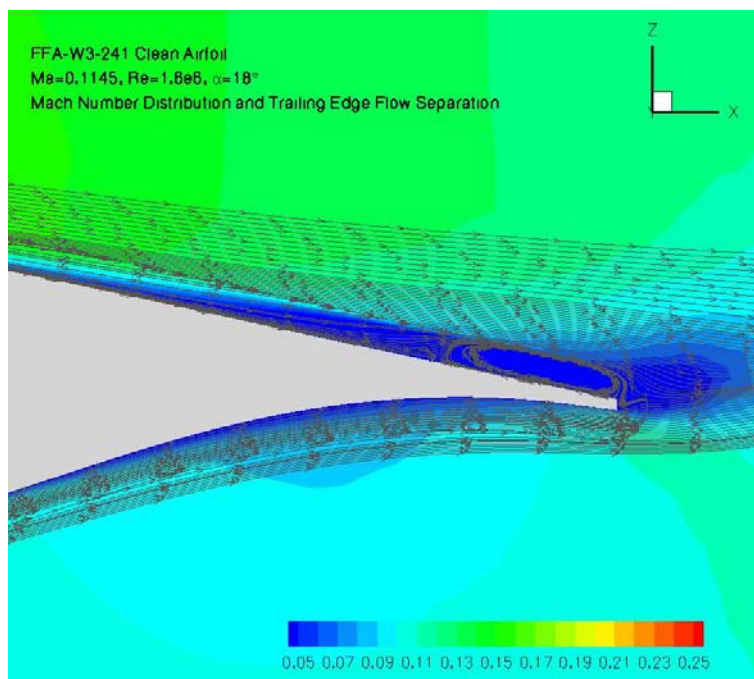

Figure 5: Trailing edge separation of the clean airfoil.

In comparison with the experimental results, the TAU computations seem to postpone trailing edge separation to higher angles of attack, since the experiments already indicate a separation developing at around 12° angle of attack. It has not been determined what

the primary cause of this tendency in the TAU results is, but the neglect of transition as well as turbulence modelling are most certainly contributing factors.
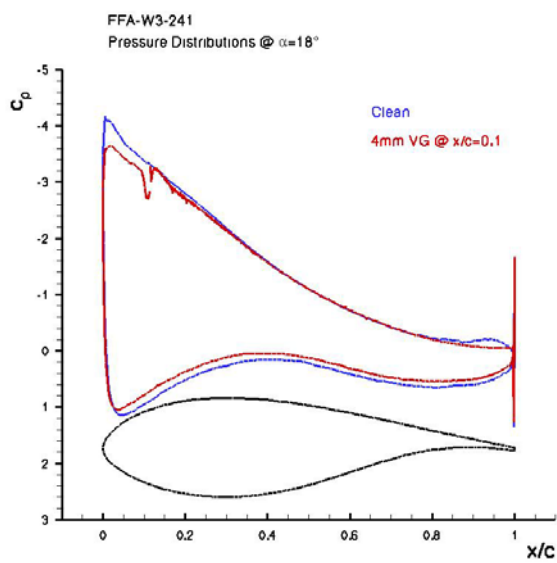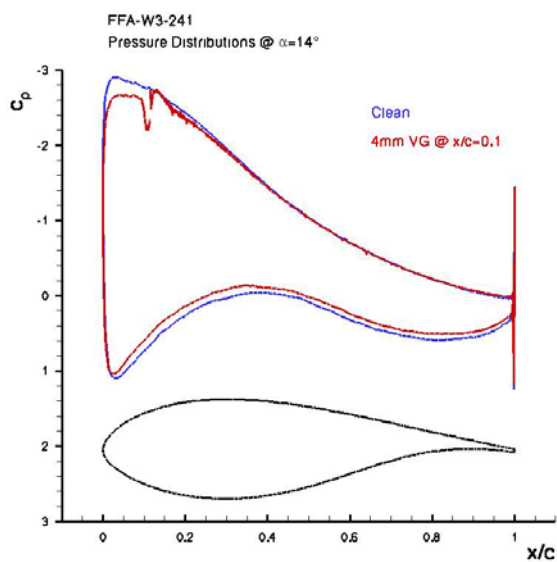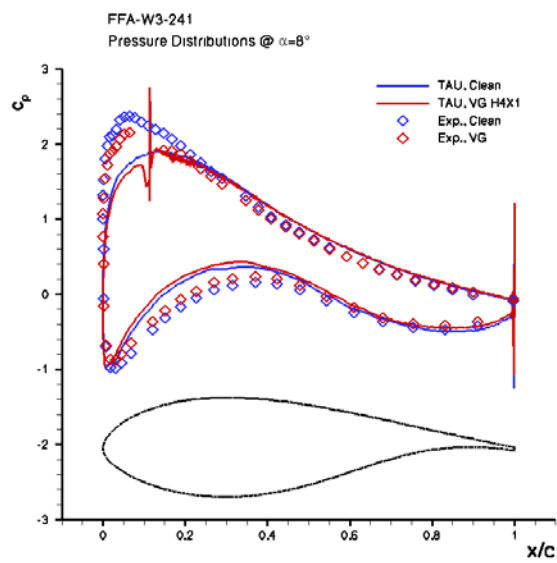

FFA-W3-241
Pressure Distributions @ $\alpha=8°$

TAU, Clean
TAU, VG H4X1
◇ Exp., Clean
◇ Exp., VG

FFA-W3-241
Pressure Distributions @ $\alpha=14°$

Clean
4mm VG @ x/c=0.1

FFA-W3-241
Pressure Distributions @ $\alpha=18°$

Clean
4mm VG @ x/c=0.1

Figure 6: Pressure distributions showing the impact of the vortex generator.

Figure 6 shows a comparison of the pressure distributions of the clean airfoil and the airfoil with VG at the three angles of attack. For the airfoil at 8° angle of attack the results from the experiments are included in the figure. Here the reduced suction peak seen at the leading edge in the CFD results seem to indicate that the accurate modelling of transition is indeed a necessity for the computations of these flows. In all three cases there is only a small impact of the VG visible in the pressure distributions. This is primarily limited to a slight reduction in the leading edge suction peak as well as to a small difference for most of the pressure side of the airfoil. This seems to be in reasonably good agreement with the trends seen in the experiments . Most importantly the CFD results show that the small separation region at the trailing edge of the clean airfoil at 18° AOA is not present for the airfoil with VG. This indicates that the TAU results properly account for the effect of the vortex generators. Figure 7 shows the vortex track and development for the case at 14° angle of attack through contours of vorticity. It can be seen that the manual grid refinement approach was successful in resolving the vortex over most of the airfoil chord.
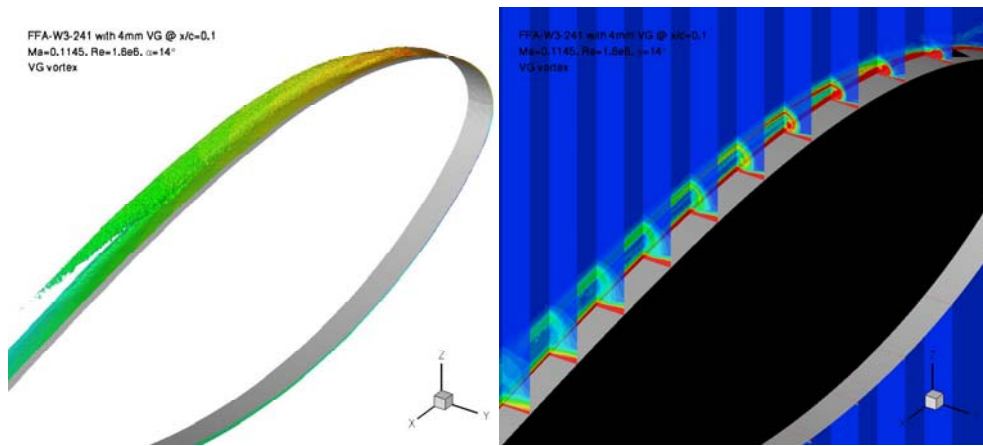

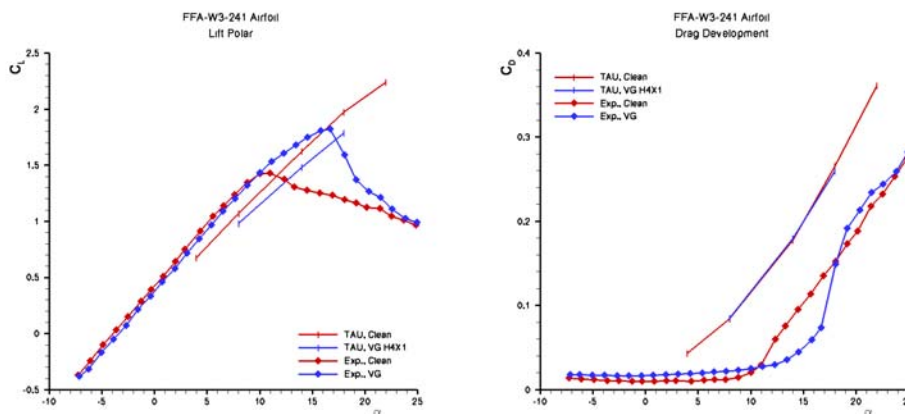*Figure 7: Vortex track and development at 14° angle of attack.*

Figure 8: Lift and drag curves for an airfoil with and without vortex generators.

Finally, Figure 8 shows the lift and drag coefficient development with the angle of attack as a comparison between the experimental and numerical results. Included in this figure are two extra data points for the clean airfoil at angles of attack of 4° and 22°. When

comparing with the trends described in ref. for the experimental investigation the TAU results for the clean airfoil show the onset of airfoil stall delayed to much higher angles of attack. As described previously notable trailing edge separation only begins to occur at around α = 18° in the CFD results and the lift curve remains linear to this angle of attack. However the reduction in lift coefficient for a given angle of attack for the airfoil with VG over the clean airfoil case seen in the experiment is also visible in the CFD results. Also, as seen in the wind tunnel tests, the differences in the lift for the two configurations increase with the angle of attack. The lift coefficients in the CFD results are generally slightly lower than the experimental values.

The differences in the drag coefficient between the two configurations are quite small and the limited numbers of angles of attack investigated make it difficult to establish a clear trend. However the drag curve does show that at the lowest angle of attack the VG case has a slightly higher drag than the clean airfoil case, while at the higher angles of attack the situation is reversed. This is in general agreement with the wind tunnel results. Drag tends to be slightly over predicted in the computations.

Discussion

The influence of vortex generators on the flow has been numerically investigated using the unstructured DLR TAU-code. With an appropriate refinement of the grid it was possible to properly resolve the vortex being produced by the VGs and to avoid early dissipation. It was shown that the CFD results seem to overestimate the angle of attack at which the airfoil stalls. It is thought that the neglect of regions of laminar flow as well as flow transition along with the impact of the turbulence model play a significant role for this discrepancy. However the reduction in lift coefficient, which is amplified at higher angles of attack, as well as the reduced drag at high angles of attack due to the influence of the vortex generator seen in experiments can also be found in the CFD results.

1.2 FORTH contribution

Vortex generator parameters

The main vortex generator parameters are the sweep angle, β, of the delta wing and the chord length c_{dw}. The incidence angle γ_{VG} is not known in advance especially for swept wings or for wind-turbine rotor blades that are usually twisted. As a result the effectiveness of the vortex generator is not the same for all incidences α of the blade. The flow field at the neighborhood of the vortex generator is quite complex and very fine grid resolution is required to capture all the details of the complex vortical flow field resulting form the vortex generator and the interaction of the helical vortex with the boundary layer flow. In this investigation, the wing is un-swept and the chord length is considered constant. The sweep angle of the vortex generator and the orientation with respect to the free stream flow direction (angle γ in Figure 9 which is the true incidence γ_{VG} for parallel flow over un-swept wing) vary. The effectiveness of a baseline vortex generator is assessed for different angles of incidence of the blade by performing RANS computations of incompressible flow with unstructured grids.
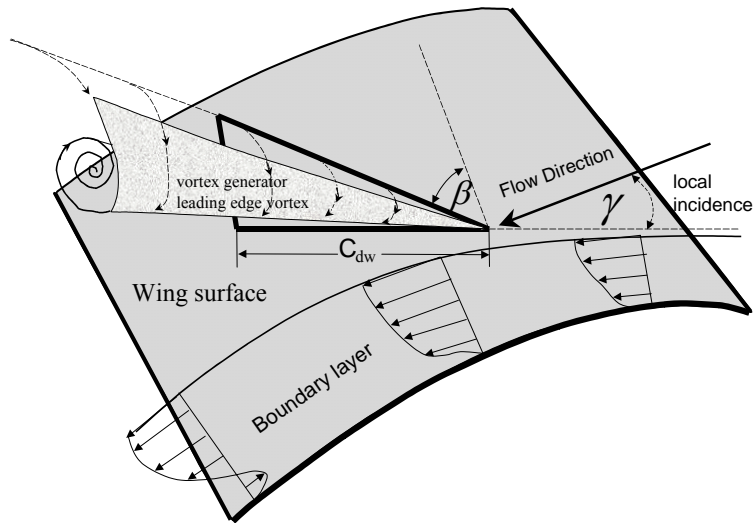
Figure 9: Schematic of a delta wing vortex generator.

Numerical Implementation

The incompressible flow equations were solved with a finite volume, cell-centered numerical method. The pressure and the velocities were collocated. In order to make possible solutions in complex domains mixed-type grid were used. For two-dimensional flows several turbulence models were used. For three-dimensional solutions were obtained with the standard k-ε model.

Computations of incompressible flow were obtained for the flow over a wing section without vortex generator control at different angles of incidence. The two- and three-dimensional results for the clean wing were in good agreement. There was also no difference between the two-dimensional results computed on structured and mixed-type of meshes. The computed flow field at $\alpha = 18°$ is shown in Figure 10.
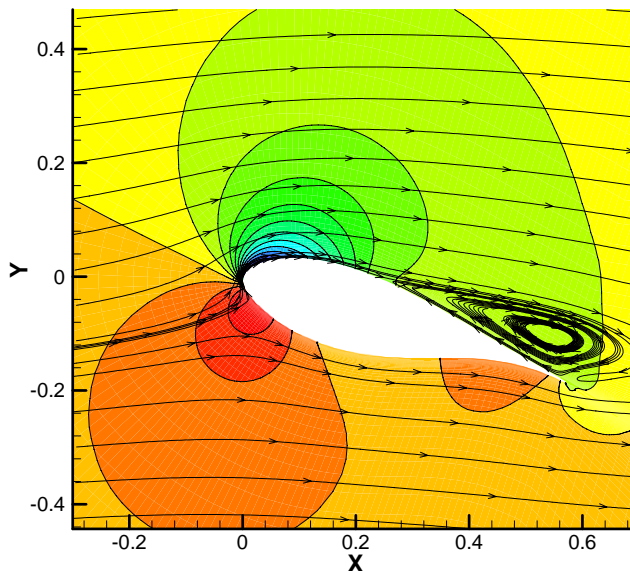
Figure 10: Computed flowfield over the wing at $\alpha = 18°$.

At incidence α = 10° the flow was found almost fully attached. At α = 14° and α = 18° there is a large recirculation zone at the wing trailing edge.

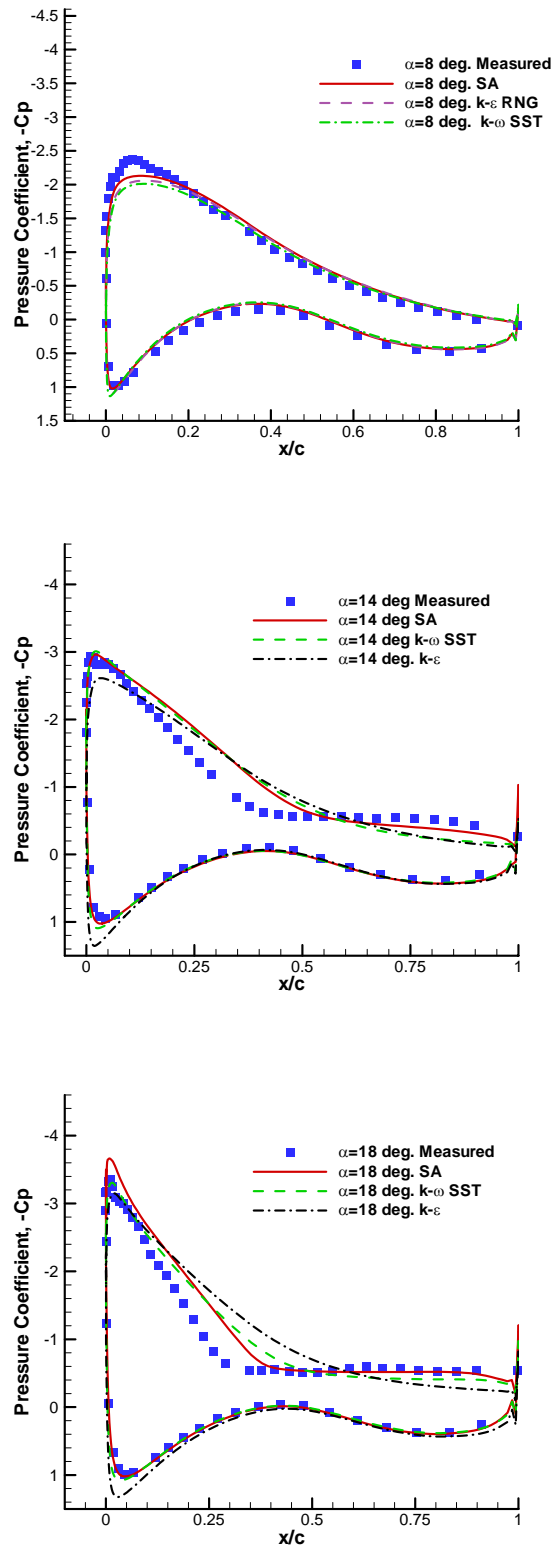*Figure 11: Comparison of the computed and measured pressure coefficient for flow without vortex generators at α = 8, 14 and 18°.*

A comparison of the computed and measured pressure coefficient distributions for the clean airfoil (without vortex generator) is shown in Figure 11. Fair agreement of the computed solution with the experiment is observed. It appears that the Spalart-Allmaras and the k-ω SST models yield the best overall agreement for both attached and separated flow.

The computations of the flow over the airfoil without vortex generator were repeated using a structured/unstructured mesh of Figure 12. For this mesh, the region of the vortex generator is discretized with an unstructured mesh with triangular elements. The computed solutions with the structured mesh with quadrilateral elements and the structured/unstructured mesh were identical.
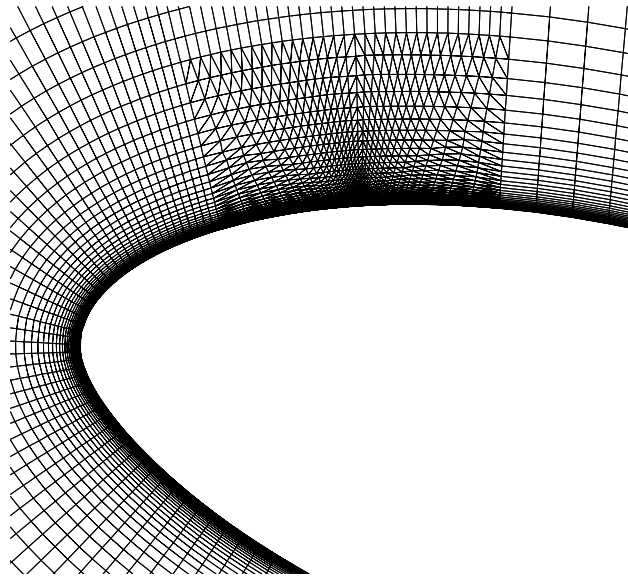
Figure 12: Structured-unstructured mesh used for the computations of the clean airfoil and computed velocity field.

The computations of the 3D flow over the wing section with the vortex generator are obtained on a structured/unstructured grid defined in the schematic of Figure 13 where the region of the unstructured mesh in the neighbourhood of the vortex generator is indicated.
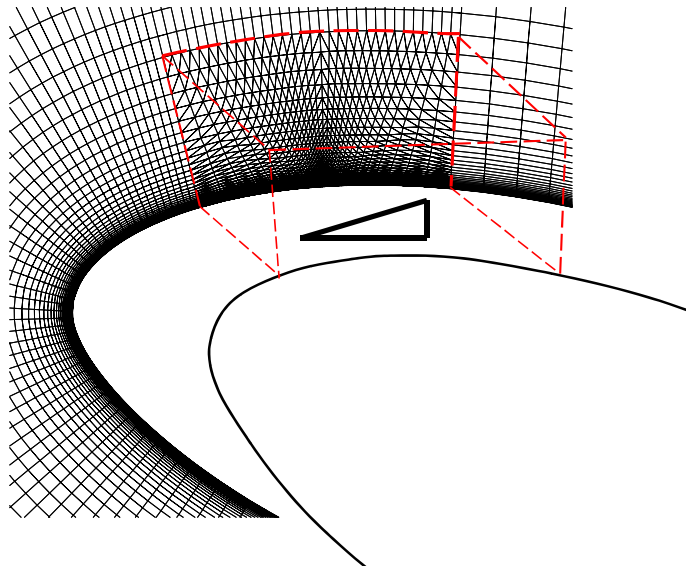
Figure 13: Schematic of 3D grid for the wing with vortex generators.

The structured-unstructured grid with the delta-wing-type vortex generator and the wing surface is shown in Figure 14. A coarse mesh with $1.9 \cdot 10^6$ vertices and $2.4 \cdot 10^6$ elements and a finer mesh with increased resolution only at the vortex generator area ($2.4 \cdot 10^6$ vertices) were used for the computations. The wing surface is discretized with a canonical structured mesh for the largest portion. Upstream and downstream of the delta wing a small buffer zone with triangular discretization of the wing surface is used. At the vortex-generator/wing junction grid clustering in both normal to the wing and normal to the vortex generator surfaces is used to provide viscous resolution for the wing boundary layer flow and the vortex generator. In the hexahedral box region around the vortex generator delta wing a mixed-type (prism/tetrahedral) unstructured grid is used to provide viscous resolution on both the vortex generator and the wing surfaces.
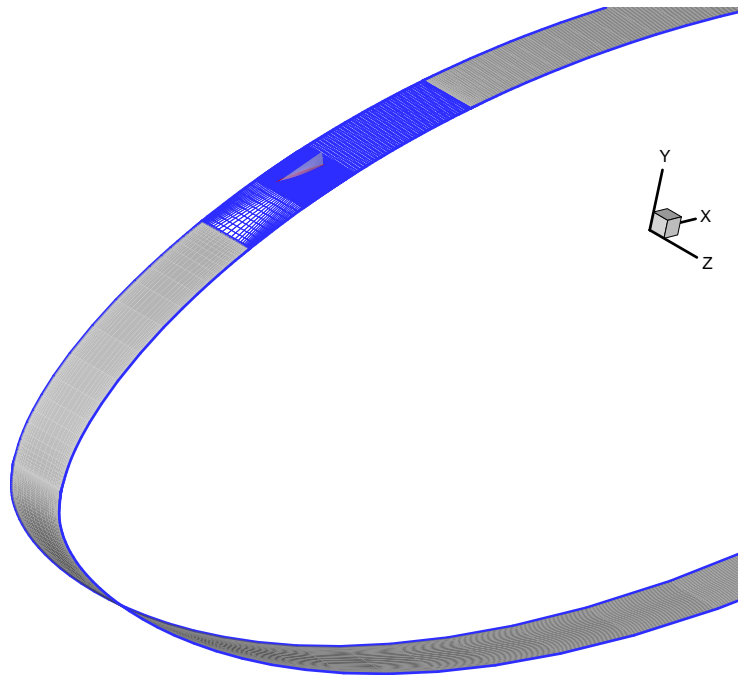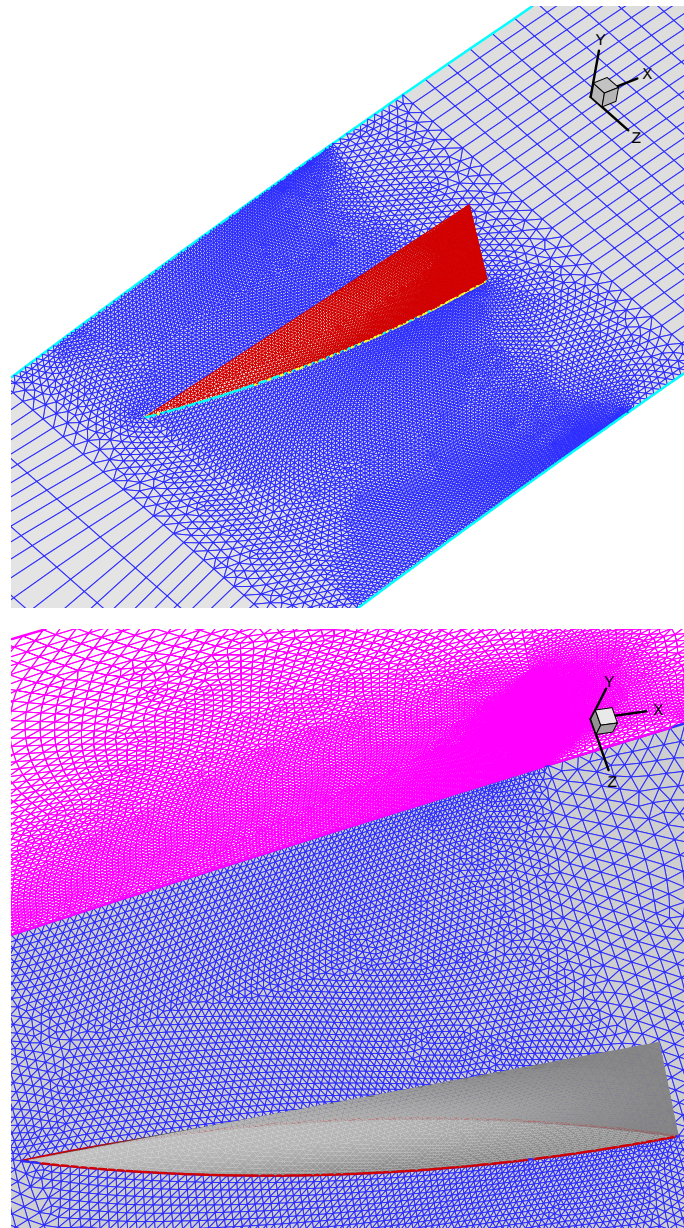

Figure 14: Structured-type wing surface grid and modified unstructured grid patch at the vortex generator neighborhood.

A prospective view of the mesh is shown in Figure 15. The top figure shows a detail of the surface meshes. The figure at the bottom shows the normal to the wing grid resolution.

Figure 15: Wing and vortex generator surface meshes (top) and viscous resolution in both normal to the wing and vortex generator directions (bottom).

At the vortex generator region the surface flow the leading edge vortex and the corner flow at the wing/vortex-generator junction is resolved with 160 intervals across the spanwise direction. The rest of the wing flow upstream and downstream of the vortex generator is computed with 30 elements in the spanwise direction. The hexahedral region enclosing the vortex generator is discretized with $3.2 \cdot 10^5$ vertices or approximately $4.0 \cdot 10^5$ elements for the coarse mesh and with almost double resolution for the fine mesh. This selection of grid topology offers the advantage of performing selective grid refinement only in the vortex generator region. The computed surface pressure coefficient distribution with vortex generator is shown in Figure 16. The flow with vortex generators was computed with the standard k-ε model. The vortex generated by

the delta wing within the boundary layer of the wing is shown in the coarse and fine grid computation of Figure 17 - Figure 20.
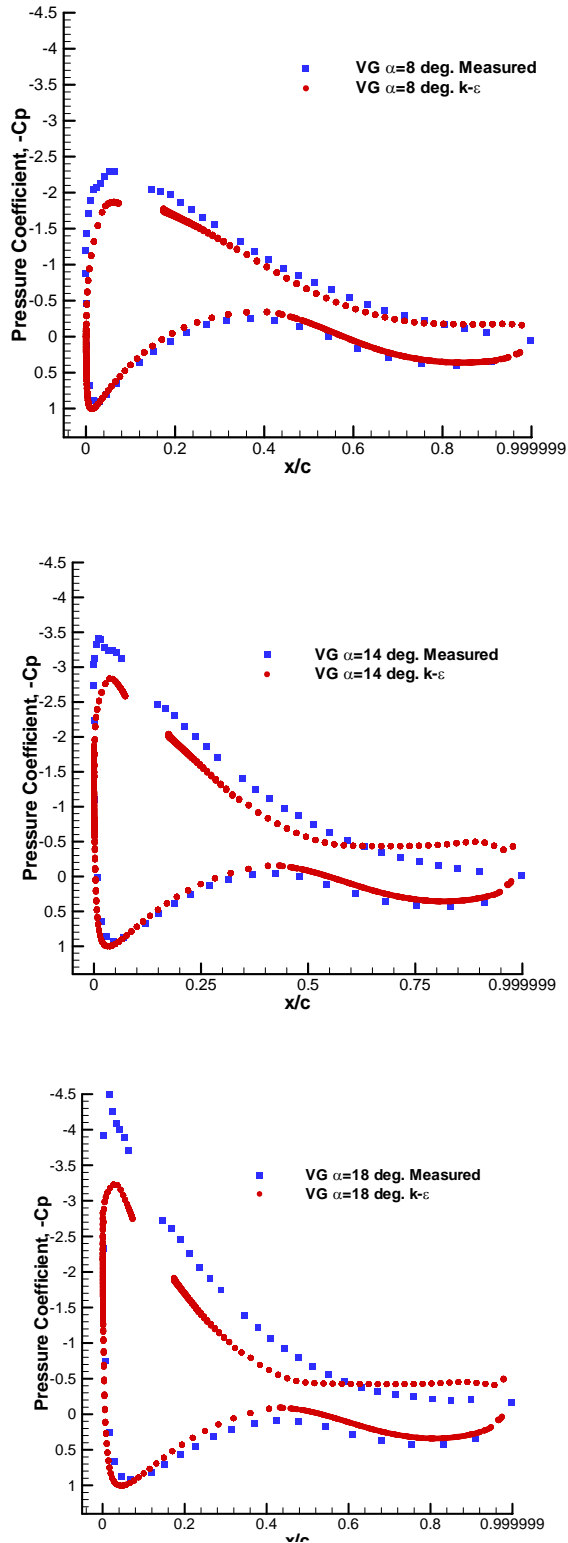

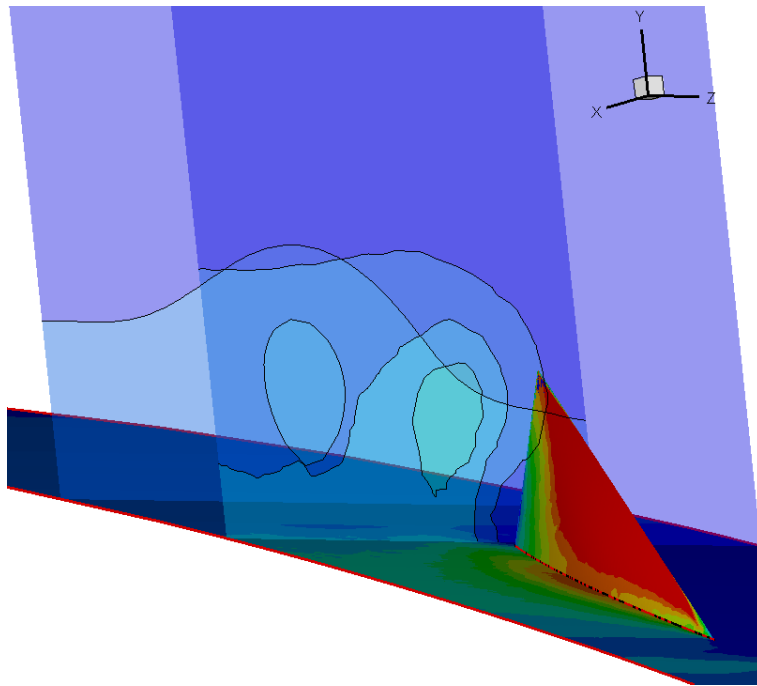*Figure 16: Comparison of the computed and measured pressure coefficient for flow with vortex generators at α = 8,14 and18°.*

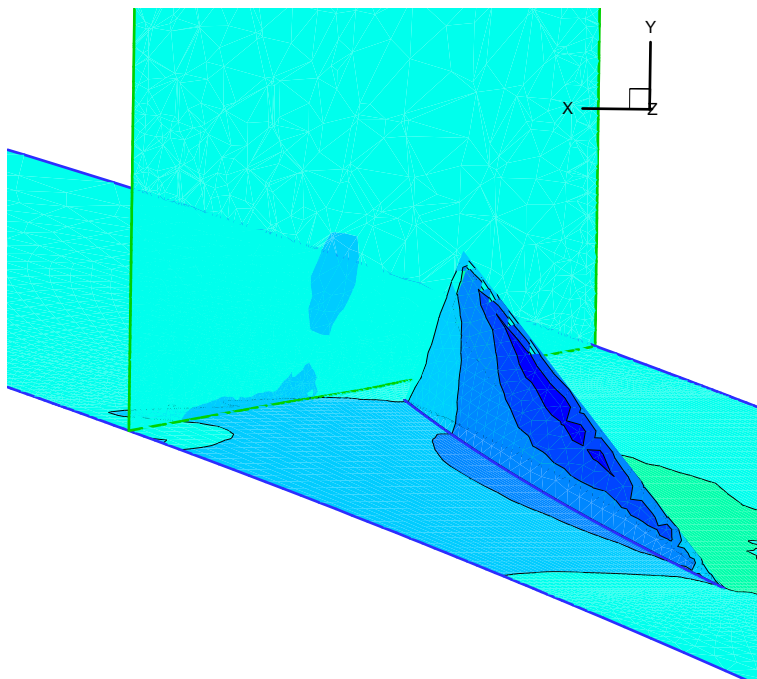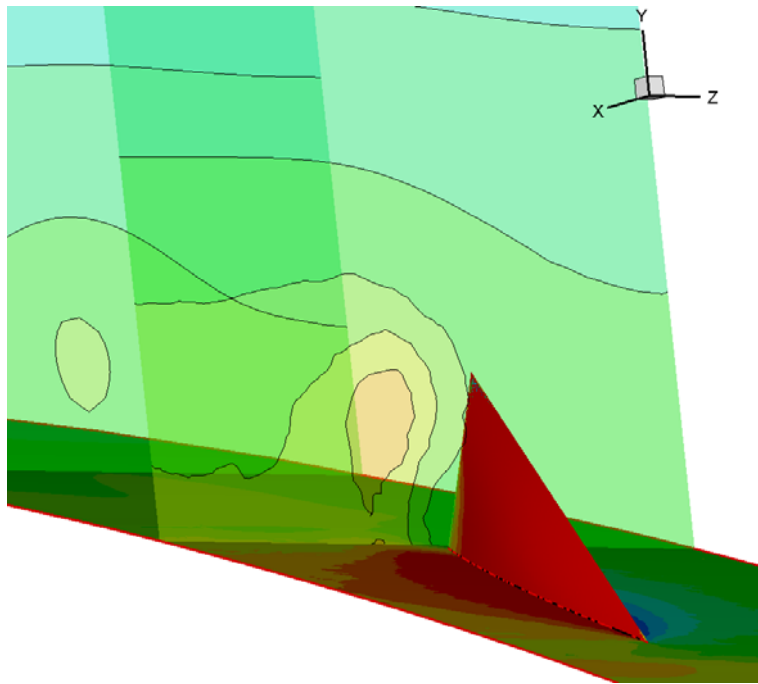*Figure 17: Computed flow field in the neighborhood of the vortex generator at wing incidence α = 8 °(fine mesh).*

Figure 18: Computed flow field in the neighborhood of the vortex generator at wing incidence α = 14° (coarse mesh).

Figure 19: Computed flow field in the neighborhood of the vortex generator at wing incidence α = 14° (fine mesh)

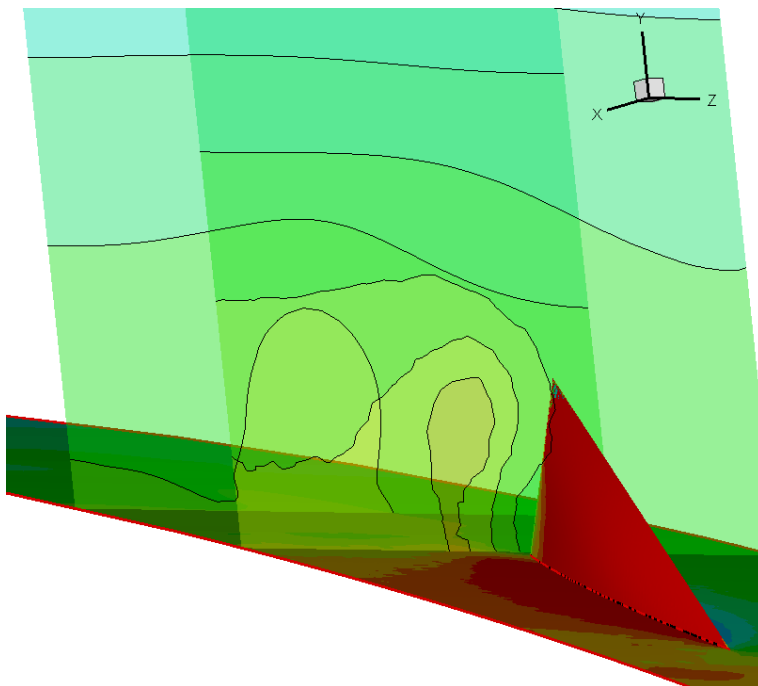*Figure 20: Computed flow field in the neighborhood of the vortex generator at wing incidence α = 18° (fine mesh).*

1.3 NTUA contribution

The investigation is based on 3D RANS computations equipped with the Spalart-Allmaras (SA) turbulence model and near-wall treatment. The VGs are modelled as thin lifting surfaces and the corresponding loading is used in constructing the extra source terms in the momentum equations. Due to the small size of the VGs, increased grid

resolution is required. To this end, the computational domain is restricted to one periodic strip of the configuration with appropriate side conditions.

The computational domain consists of an orthogonal curvilinear staggered grid covering one period of the VG layout. Considering the small span width of the blade slice, it is assumed that the cross section remains the same. Over the cross sections of the blade a C-type grid is used. The finite volume method is adopted and the hybrid convection-diffusion model using the SIMPLE pressure correction scheme. Turbulence closure is based on the SA model, while transition modelling uses the Michel criterion.

The source term model for VGs

In view of obtaining a computationally efficient model, the presence of the VG is taken into account through the body forces exerted on the fluid. The VG is considered as a thin-lifting surface and so the body force considered is that of the lift. With reference to Figure 21, the angle of attack can be approximated as: $\alpha = (\vec{U} \cdot \vec{n}) / |\vec{U}|$ where $\vec{U}$ denotes the local velocity. For a rectangular $\vec{b}$ will denote the direction of the bound vorticity Γ. Then using Joukowski's theorem, the lift force can be approximated as:

$$\Delta \vec{L} = \rho (\frac{\vec{U}}{|\vec{U}|} \times \vec{b})(\vec{U} \cdot \vec{t}) \Gamma \Delta \ell ,$$

where $\Delta \ell$ denotes the length of the vortex. By relating α and Γ according to linear theory, the lift on a part of the VG with surface ΔS will be given as:

$$\Delta \vec{L} = c \rho (\frac{\vec{U}}{|\vec{U}|} \times \vec{b})(\vec{U} \cdot \vec{t})(\vec{U} \cdot \vec{n}) \Delta S ,$$

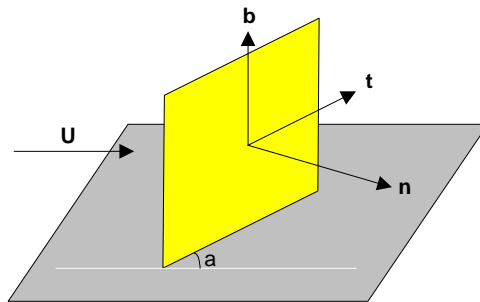where c is a constant related the lift slope of the VG and is subjected to calibration.

Figure 21: Geometry definitions of a VG

The computed lift force is added to the discretized momentum equations as an extra source term. The source term is invoked for the cells containing the VG. In this connection the details of the geometry of the VG are used. The grid being orthogonal, it is clear that in case of a swept VG, its geometry will be approximated by a stair-case like line.

Computational details

The total number of grid nodes was approximately 720.000, including half of a VG pair. A detailed resolution in the spanwise direction has been adopted (the physical distance is

about 1.25mm for the fixed wing tests presented) in order to capture the streamwise vortex as well as the secondary produced flow due to VG's. Approximately 80 cells were used to resolve the VG to be modelled. This was based on the experience acquired from modelling air-jet VG's [8], where a similar secondary flow is developed.

Due to the small size of the vortex generators, the computational domain is restricted to one periodic strip of the configurations with appropriate side conditions. In particular:

- For contra-rotating orientation of the VG pair, symmetry conditions were applied, whereas

- For co-rotating orientation of the VG pair, cyclic conditions were applied.

Results

The VGs modelled have the shape of orthogonal triangles (according to the description of the experiment on the FFA-W3-241 section, ref.) and they are placed with their right angle perpendicular to the airfoil surface. They are placed so that their height increases towards the trailing edge. VGs are arranged in pairs at equal and opposite angles relative to the chord of the blade. In particular, the VG being modelled has a length of 18mm, a height of 6mm, a planform area of $54mm^2$, $\pm19.5°$ angles of attack relative to the external flow and a tilt angle of 90° to the blade surface. The leading edge spacing between two VGs is 10mm and the distance between two consecutive pairs is 25mm. Thus, the total spanwise distance, which a VG pair occupies, is 35mm. Two sets of tests have been performed: the first concerns the performance of VG's performance on a fixed wing configuration corresponding to the available measured data, ref. , and the second the case of a rotating blade, which will be described in the following Section 2.

For the fixed wing configuration, the experiment on the FFA-W3-241 section at 14.4^o of incidence and a Reynolds number equal to $1.6 \cdot 10^6$ has been simulated in different configurations including VGs' chordwise placement and arrangement. Moreover, for the case in which the VGs are placed at x/c=20%, simulations have been performed over a wide range of incidences (see Table 2).

Table 2: Fixed wing configuration runs

aoa (deg)	VGs' position (%c)	VGs' arrangement
5	20	Contra-rotating
10.2	20	Contra-rotating
12	20	Contra-rotating
14.4	10	Contra-rotating
14.4	20	Contra-rotating
14.4	30	Contra-rotating
14.4	30	Co-rotating
16	20	Contra-rotating
19	20	Contra-rotating

As a validation of the flow solver, the cases of 10.2 and 16° of incidence without VGs were simulated. In Figure 22 the corresponding pressure distributions are compared to measurements and other predictions taken from ref. .
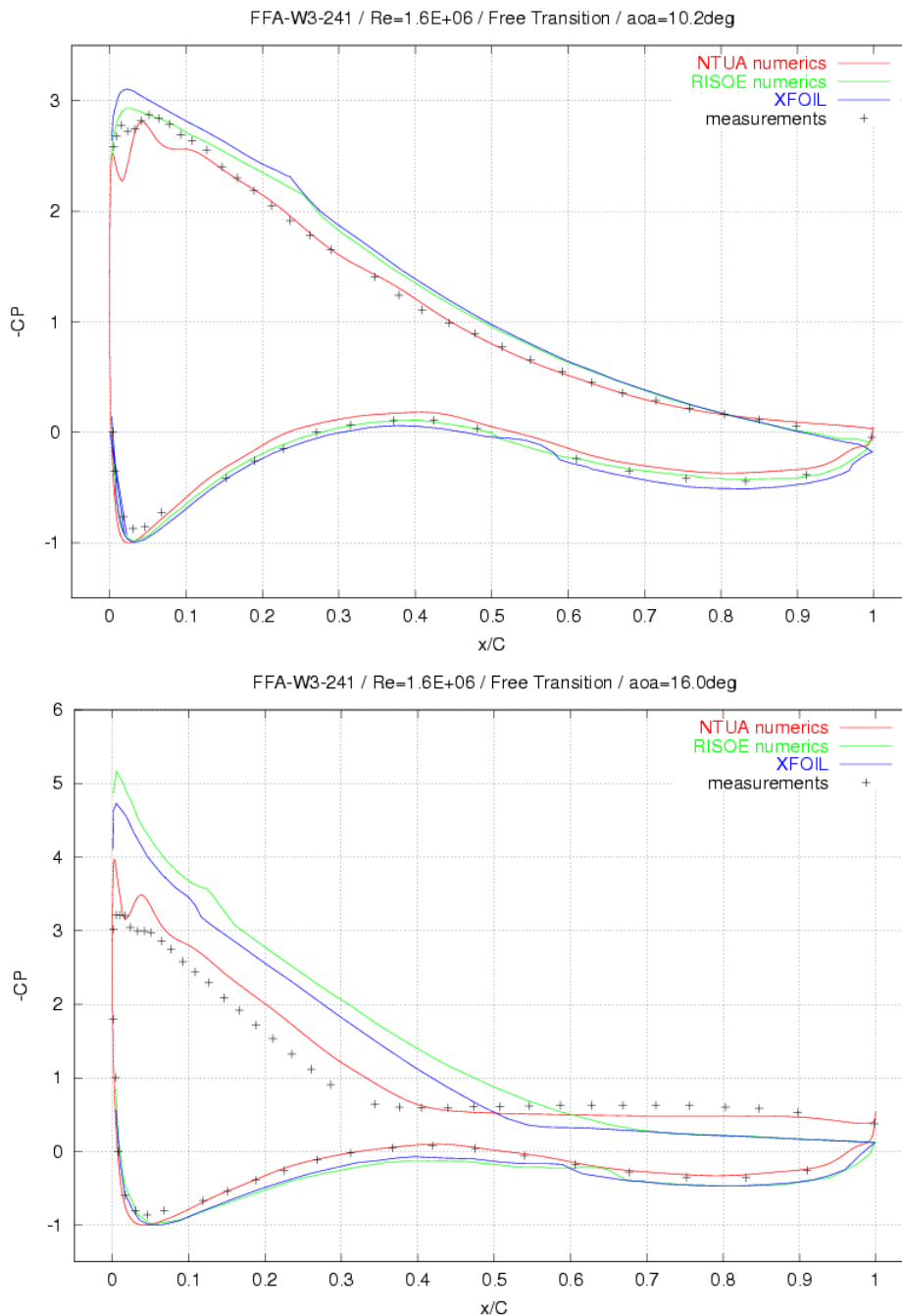

Figure 22: Pressure distributions on the FFA-W3-241 wing section without VGs at 10.2 and 16° of incidence.

In these simulations the airfoil shape was taken by digitization and corresponds to the actual model geometry. This probably explains the better correlation of the NTUA results with measurements. Although transition is not a point specifically considered in this work, it is noted that the location is well predicted in NTUA's results. In summary, these results indicate that up to stall the model performs well. Beyond that point the code will over predict lift, which is a well-known deficiency of RANS codes.

Next as an introduction to the remaining results two figures from ref. are presented.
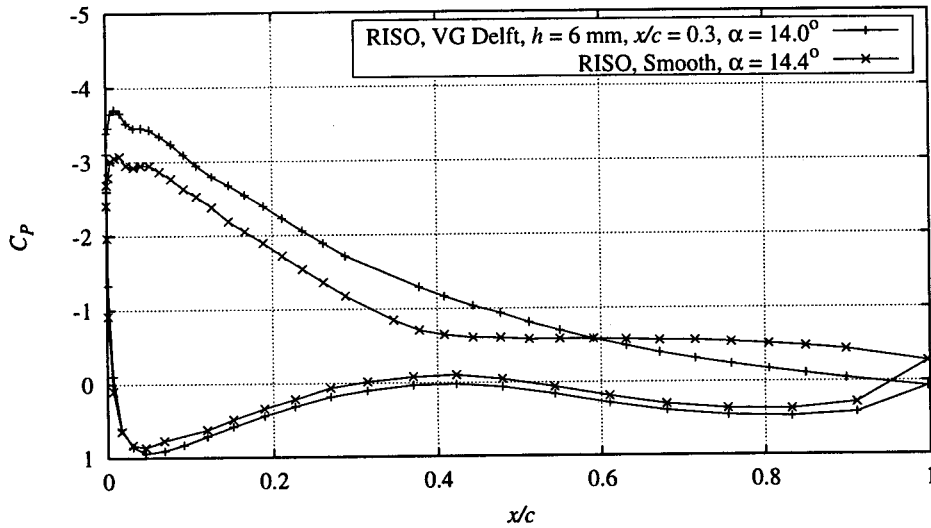
Figure 23: Measured pressure distributions on the FFA-W3-241 wing section with and without VGs at 14° of incidence. From ref. .
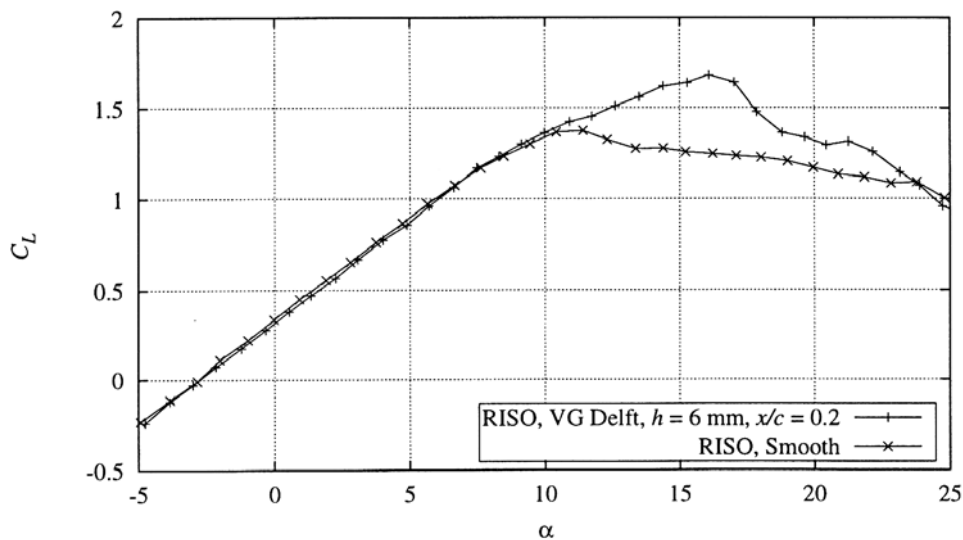
Figure 24: Measured lift coefficient distributions on the FFA-W3-241 wing section without and with VGs located at x/c=20%. From ref. .

Figure 23 shows the comparison in terms of pressure distributions with VG at x/c=30% with respect to the smooth case as measured during the wind tunnel tests at ~14° of incidence. It is clearly seen that the presence of the VGs cancels the onset of separation and increase the suction peak leading to higher lift.
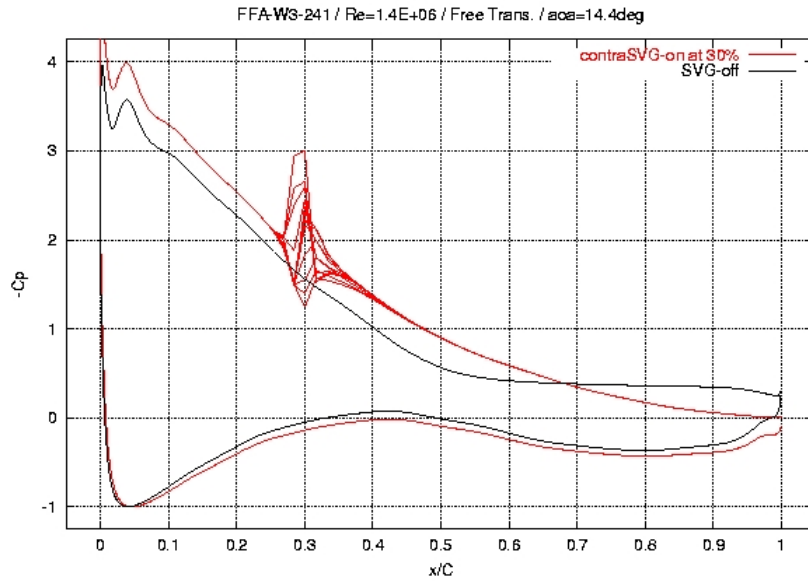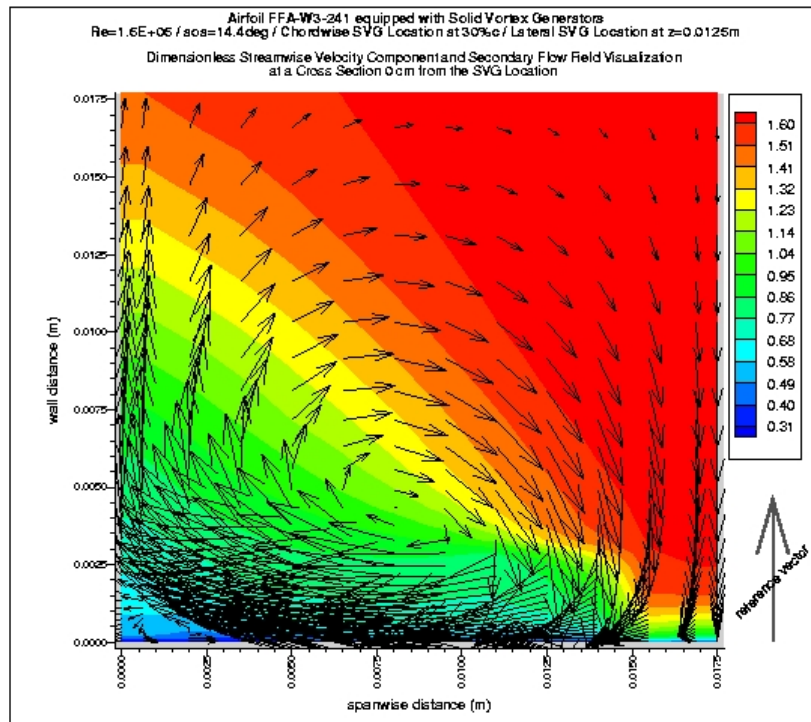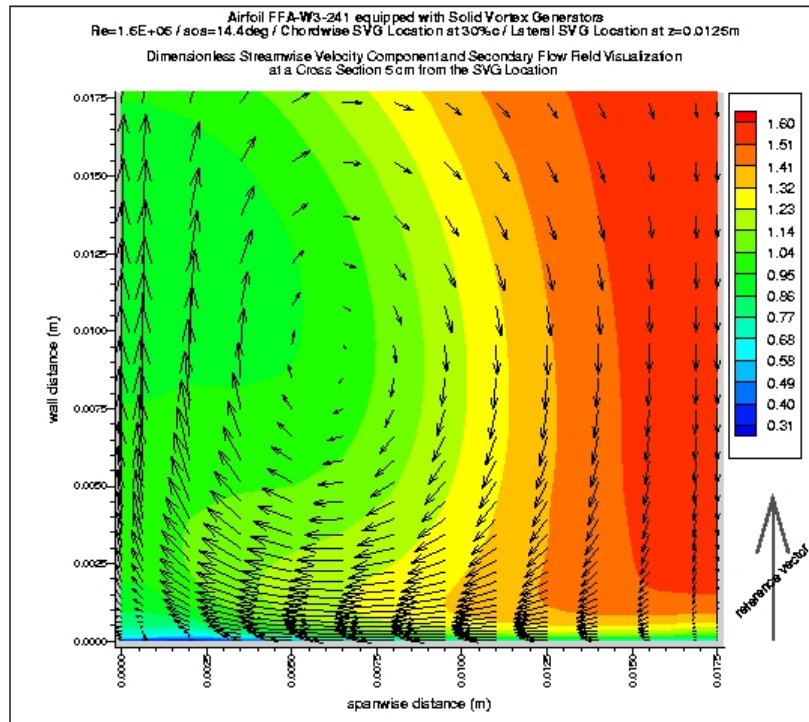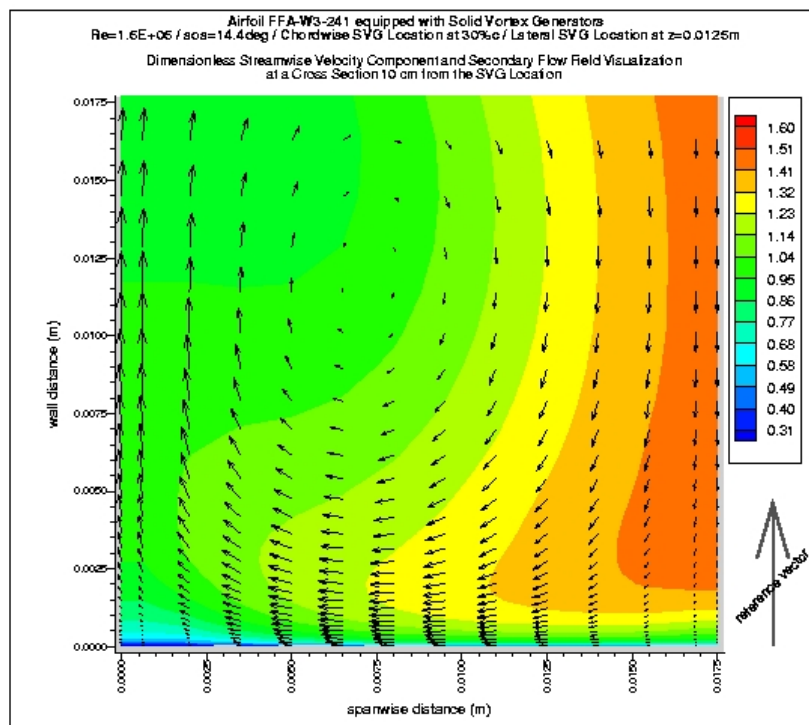
Figure 25: Predicted pressure distributions on the FFA-W3-241 wing section with and without VGs at x/c= 30%, $\alpha = 14.4^{o}$ of incidence, case of contra-rotating lay-out.

The predicted results, corresponding to Figure 22, are shown in Figure 25. Comparing the two results, qualitative agreement is found. Separation is cancelled and accompanied by higher suction pressures over the entire suction side. From a quantitative aspect, the predicted length of the separation bubble is shorter and this explains why there is an over prediction of pressure. Otherwise the amount of increase in $-C_P$ is similar.
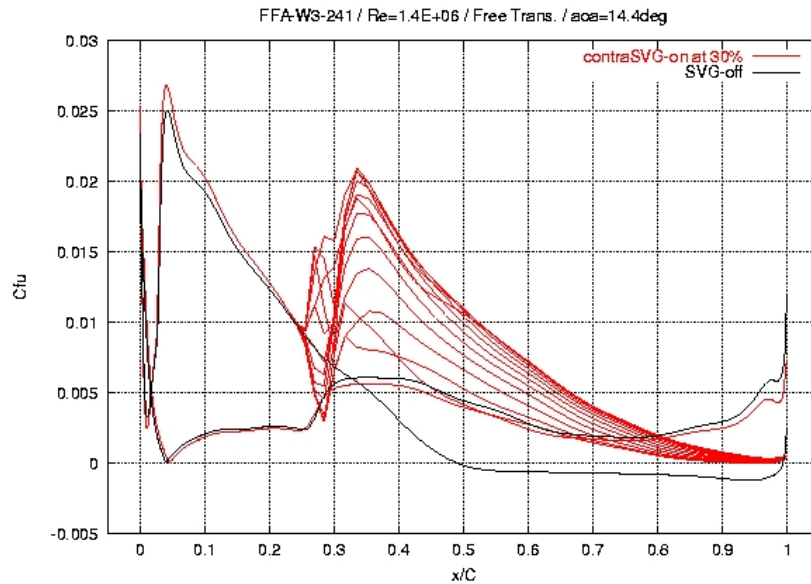
Figure 26: Predicted friction distributions on the FFA-W3-241 wing section with and without VGs at x/c= 30%, $\alpha = 14.4^{o}$ of incidence, case of contra-rotating lay-out.

The cancellation of separation is clearly seen also in the friction distributions shown in Figure 26. Note that in Figure 25 and Figure 26 all spanwise stations are shown. In the pressure distributions the differences are localized at the location of the generators whereas in the friction distributions the differences are extended over the entire chord length. Finally, on the pressure side and at the region of stagnation, a small shift is seen in the measurements, which is not so pronounced in the predictions. One possible reason is the global effect the tip vortex on the effective angle of attack. Clearly the predicted upstream effect, in this particular case is smaller as compared to measurements. In this connection some insight can be obtained from cross-sectional velocity vector plots. In Figure 27 such plots are shown for various stations indicated by the distance Dx/c from the VG. In these plots contours of the streamwise velocity are also shown. The vortex just downstream the VGs is strong and calculations show that it remains concise for approximately 15% of the chord length.
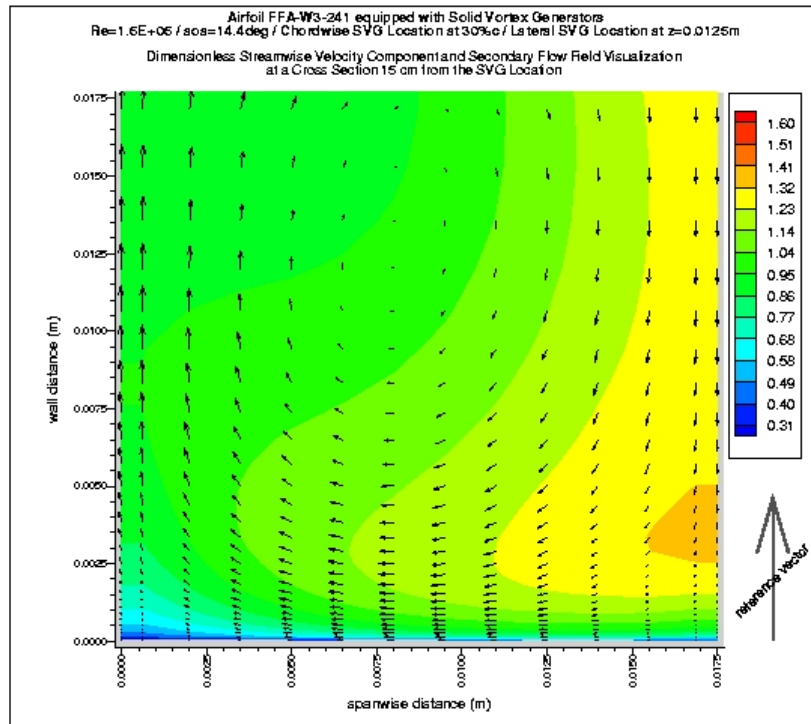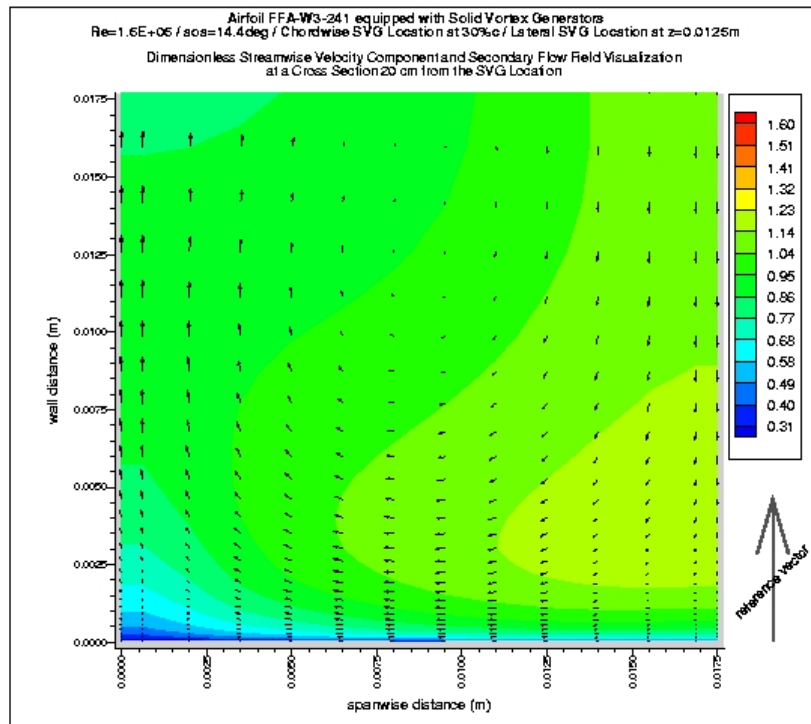

(a) Dx/c=0 (just after the VGs)

(b) Dx/c=5% after the VGs

(c) Dx/c=10% after the VGs

(d) Dx/c=15% after the VGs

(e) Dx/c=20% after the VGs

Figure 27: Cross flow vector plot and contours of the streamwise velocity component just after the VGs, case of contra-rotating lay-out.

Next, in Figure 28 the co-rotating case is presented for the same incidence.
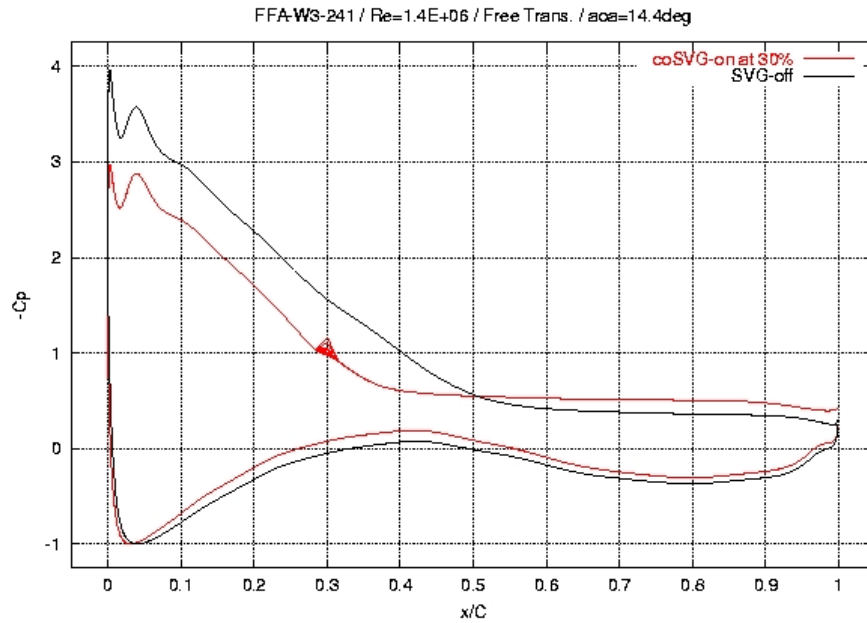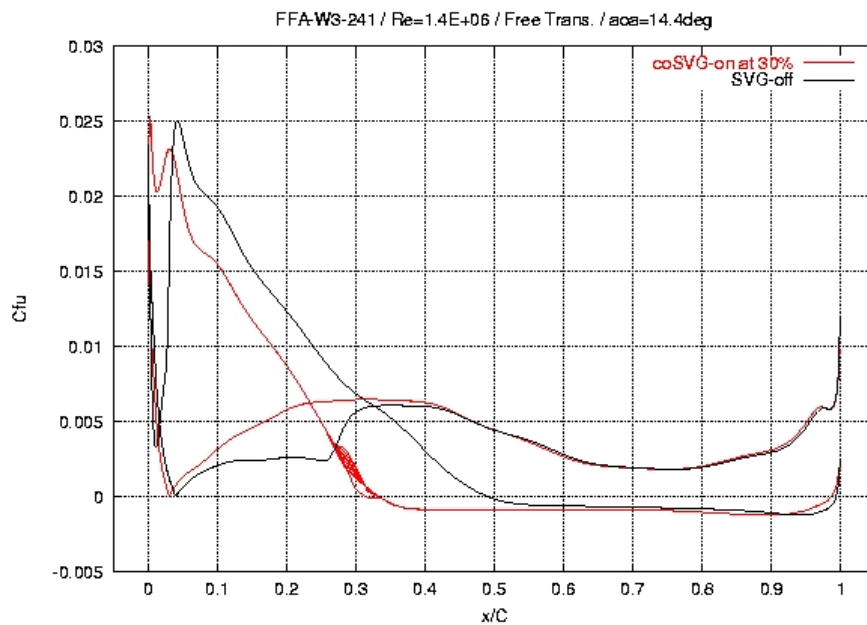
Figure 28: Predicted pressure distributions on the FFA-W3-241 wing section with and without VG at x/c= 30%, α = 14.4° of incidence, case of co-rotating lay-out.
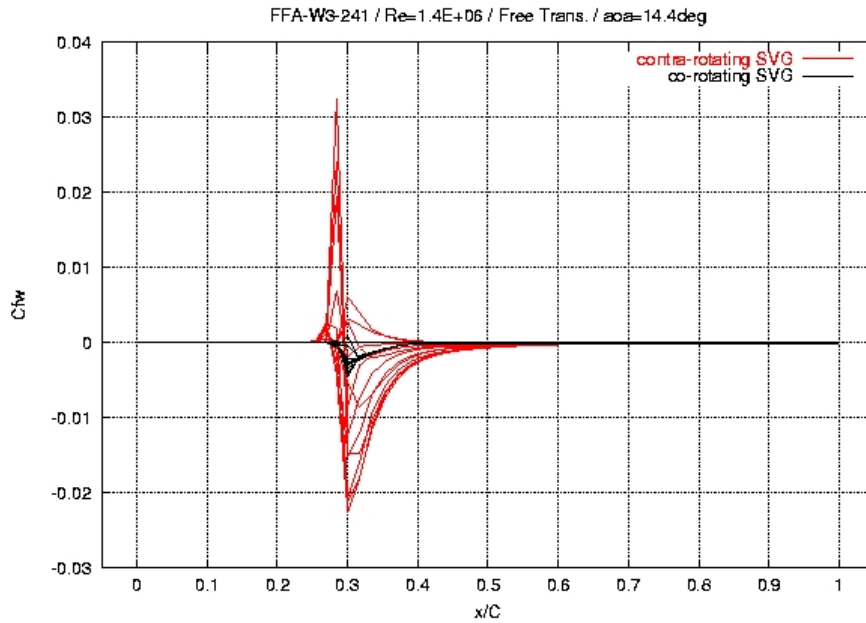
It is clear that a negative effect is produced by the presence of the VGs. Instead of increasing the lift, VGs will degrade the performance of the airfoil by increasing the extent of the separation bubble (Figure 29).

Figure 29: Predicted friction distributions on the FFA-W3-241 wing section with and without VG at x/c= 30%, α = 14.4° of incidence, case of co-rotating lay-out.

Figure 30: Predicted cross friction distributions on the FFA-W3-241 wing section for co- and contra-rotating VG layouts placed at x/c=30%.

In Figure 30 the cross friction coefficient is shown for the two VG layouts. In the contra-rotating case the generated vortex is significantly stronger which explains the beneficial effect this layout has on the performance of the section.

Also ineffective is the positioning of the VGs far from the separation. This is shown in Figure 31 and Figure 32 corresponding to the placement of contra-rotating VGs at x/c=10%.
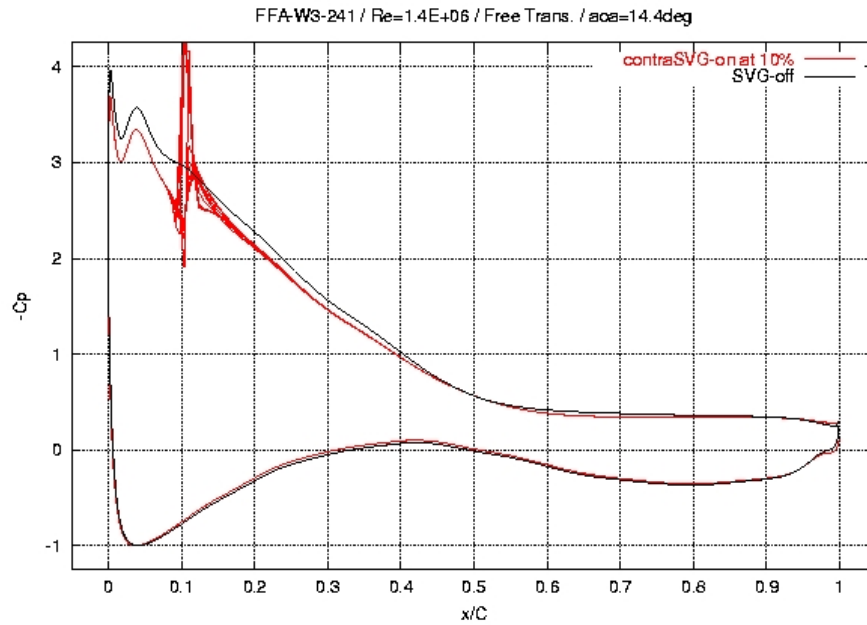
Figure 31: Predicted pressure distributions on the FFA-W3-241 wing section with and without VG at x/c= 10%, α = 14.4^o of incidence, case of contra-rotating lay-out.

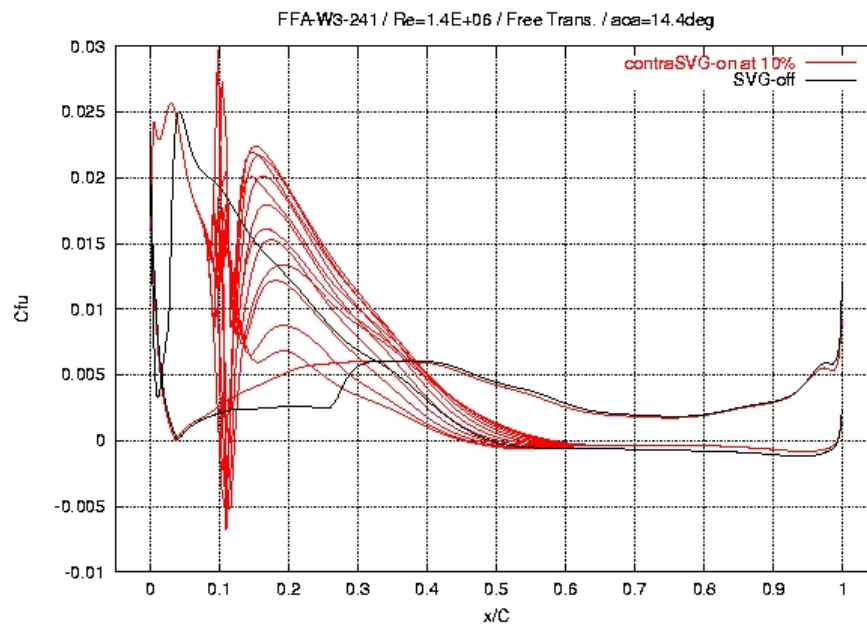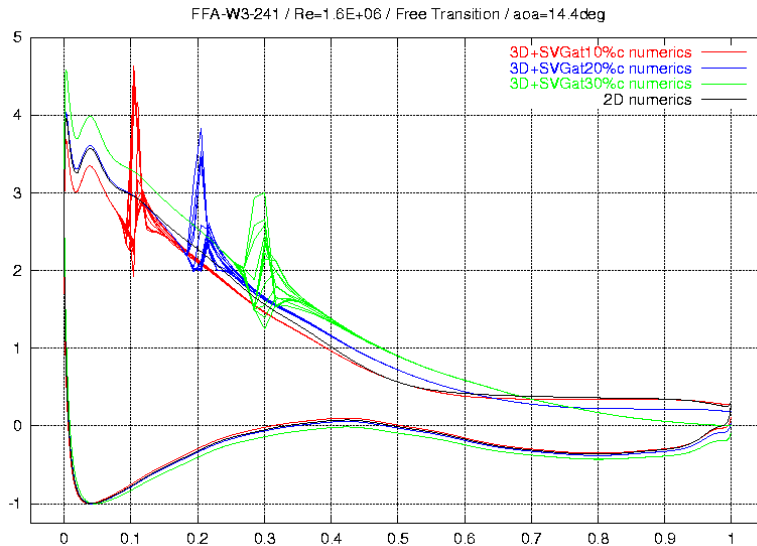*Figure 32: Predicted friction distributions on the FFA-W3-241 wing section with and without VG at x/c= 10%, α = 14° of incidence, case of contra-rotating lay-out.*

Figure 33: Predicted pressure distributions on the FFA-W3-241 wing section at α = 14.4º of incidence, with VGs located at various chordwise positions, case of contra-rotating lay-out.

In Figure 33 the pressure distributions are shown for three different chordwise placements of the VGs. Clearly the effectiveness of VGs will increase as they approach the point of separation. In this respect, it is noted that the downstream distance, where the secondary vortex develops in a confined way, ranges from 19% chord to 28% chord, when VGs placement with respect to the leading edge ranges from 10% chord to 30% chord respectively. So it follows that the chordwise location of the VG's is the most significant parameter for their performance.
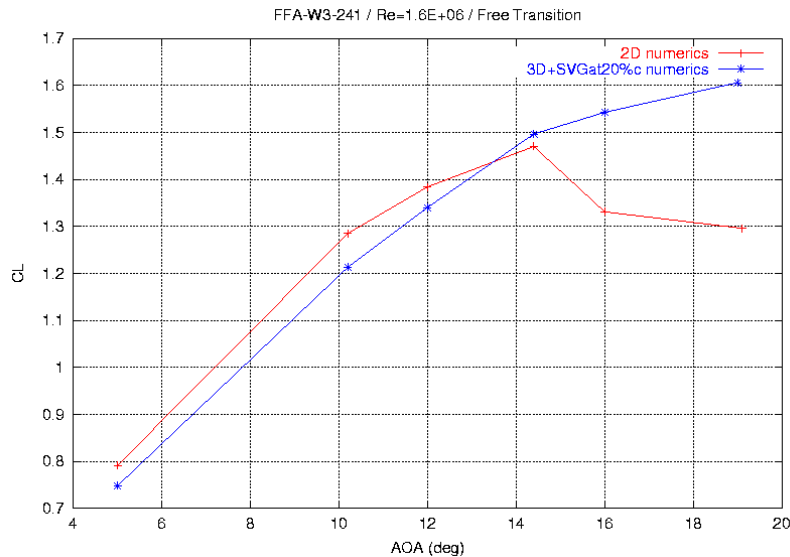

Figure 34: Predicted lift coeficcient distributions on the FFA-W3-241 wing section, with and without VGs located at x/c=20%, case of contra-rotating lay-out.

Finally, in Figure 34 the lift curve for the case of contra-rotating VGs placed at x/c=20%, is compared to prediction without VGs. As in the measurements (see Figure 22), the presence of the VGs produces the same effect in the RANS computations: improvement of the performance for incidences, which correspond to the non-linear part of the C_L

curve. It is noted however that with VGs in place, there is a shift in the zero-lift angle. This is attributed to the overall effect of the vortex on the effective angle of attack. In the case already discussed this effect could not be clear, since the cut-off of separation masked this effect. In fact if an incidence of 10.2^o is considered, the presence of VGs will give in the predictions a negative effect (Figure 35). Focusing on the stagnation region, a decrease in incidence is found. In the modelling considered, the conditions far from the airfoil are set from a potential calculation without considering the presence of the vortex. So an improvement would be to include the vortex when calculating the upstream inflow conditions.
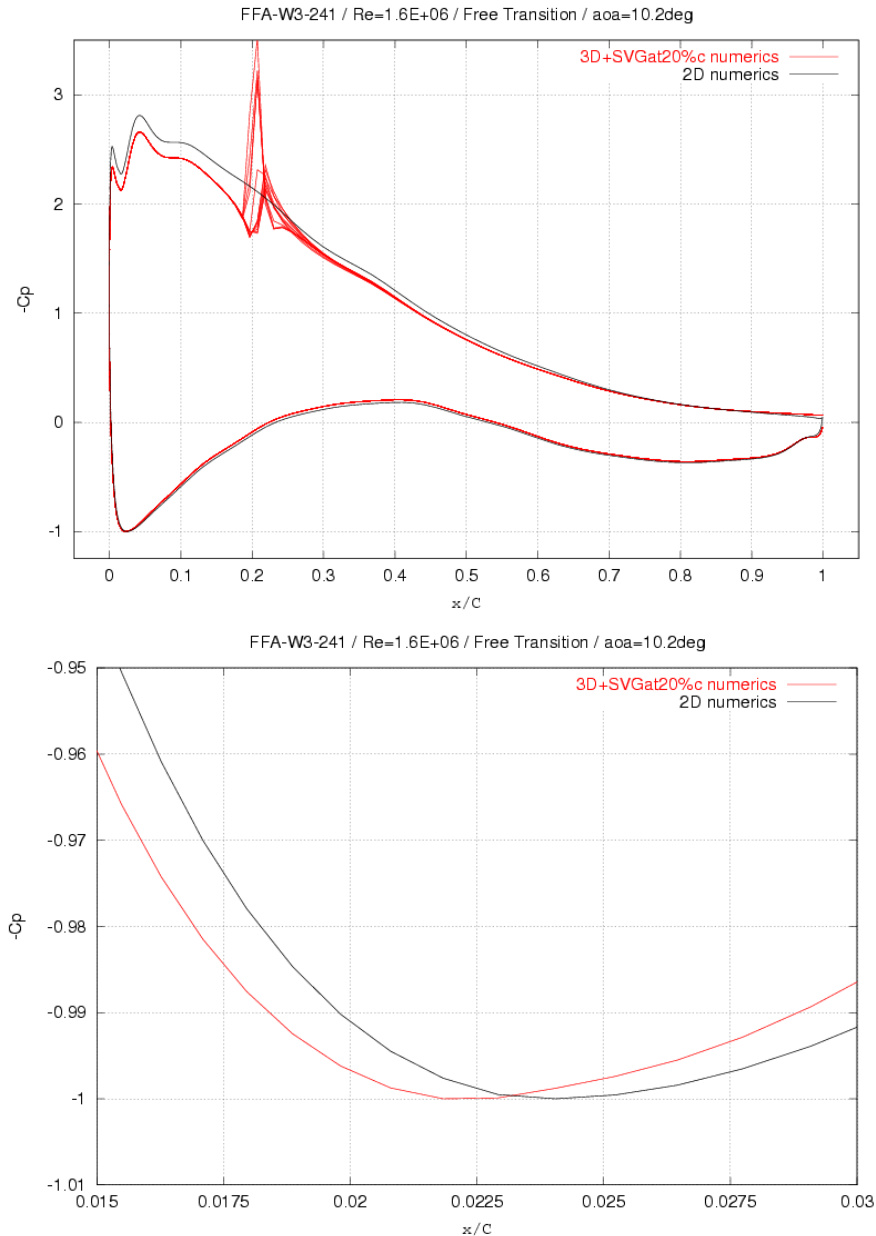

Figure 35: Predicted pressure distributions on the FFA-W3-241 wing section with and without VGs at x/c= 20%, $\alpha = 10.2^o$ of incidence, case of contra-rotating lay-out.

1.4 DTU contribution

DTU implemented the technique denoted Immersed Boundaries in the EllipSys3D code[9], [10] and [11] and applied this to model the presence of the vortex generators (VGs) [12]. In Immersed Boundaries the presence of a wall is modelled by adjusting volume forces in the computational grid that ensures the no slip condition to be fulfilled at the location of the wall, i.e. the geometry of the wall is not directly resolved in the grid. However, the grid surrounding the wall needs to be able to resolve the wall sufficiently and thus in the case of the VGs, with a height of only approximately the boundary layer thickness on the blade, needs to be very fine around the location of the VGs. The geometry of the wind turbine blade section is resolved using a structured body fitted mesh. Due to the very large number of cells needed near the VGs only one set comprised by two closely spaced vortex generators are modelled. The two vortex generators are placed so that they create two contra rotating vortices. Since only one set of VGs is simulated the effect is very local and is expected to only give a very minor change of the global characteristics to the blade section. It is expected that the two main vortices will induce two secondary vortices as sketched in Figure 36.
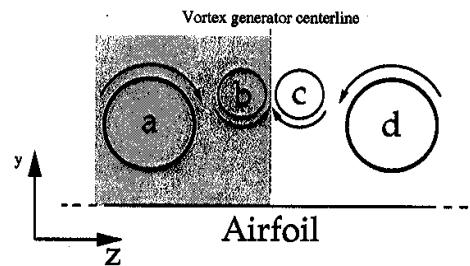

Figure 36: A sketch of the expected vortex system behind the two closely spaced VGs generating two contra rotating vortices (a and d) that induce two secondary vortices (b and c).

Two different test cases were examined. First the FFA-W3-241 airfoil with vortex generators was computed and secondly a more generic case of a bump mounted in a low speed wind tunnel. In the latter case Stereoscopic Particle Image Velocimetry, SPIV, measurements were also done at MEK/DTU with and without a set of VGs attached on the top of the bump in order to validate the capability of the Immersed Boundary technique to model VGs. A CD-R describing the experiment and containing the results will be made available to the partners.

The FFA-W3-241 airfoil

To compute the FFA-W3-241 airfoil at an angle of attack of 14° a (24 block$\times 64^3$cells/block=6.29 mill cells) grid was used to cover a two-chord long blade section. Conventional in and outlet boundary conditions are used on the up- and downstream boundaries, whereas symmetry boundary conditions were applied on the lateral boundaries. Due to the large number of cells required to resolve the VGs, only one pair consisting of two contra rotating VGs are simulated in the mid span. The computational cells are stretched towards the middle to have a better spanwise resolution around the two VGs. The VGs are placed at a chordwise position of x/c=0.1. The

geometries are semi delta shaped with a length l/c=0.0111 and a height h/c=0.0067. The leading edge spacing is sl/c=0.010 and their trailing edge spacing is st/c=0.018, which give them an angle of attack with the chordwise flow of 21°. The flow was modelled using RANS, DES and LES. The grid is, however, much to coarse for LES computations so these results should be taken with great care. In Figure 37 are shown near wall u-velocity contours for negative values ranging from –0.1(blue) to 0.0(red). u is the velocity component in the chordwise direction.

| RANS | DES | LES |
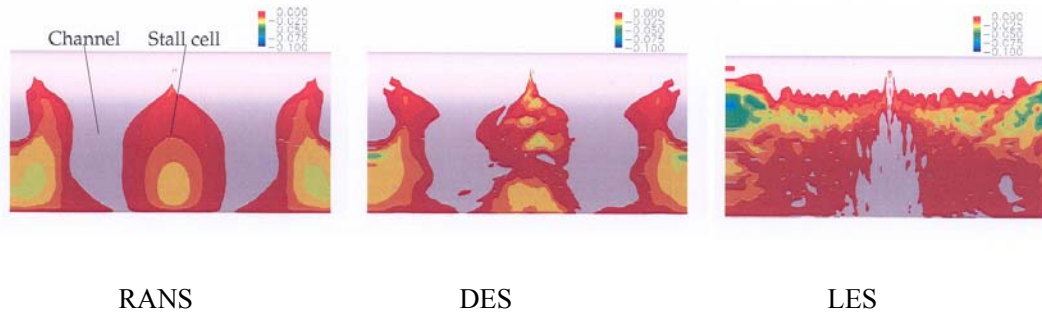
Figure 37: FFA-W3-241 with vortex generators, seen from above and with flow coming from the top. Near wall u-velocity contours, shown only for negative numbers, –0.1(blue) and 0.0(red).

For both RANS and DES there seem to be stall cells on the blade section, where the flow is actually separated behind the VGs and flow is funnelled in channels beside the VGs. This is not what is expected from VGs, which are expected to reduce separation in their wake, which is actually observed in the LES result. However, the mesh is much to coarse for LES computations, so provided that the immersed boundaries can simulate VGs the flow is more likely to be as predicted by RANS or DES. The immersed boundary technique is actually producing a vortex system as expected from Figure 36, see Figure 38, but the strength of the vortices might be too small to prevent separation.
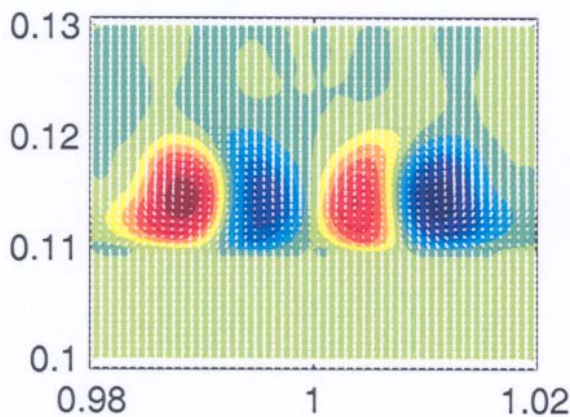

Figure 38: RANS simulation. v and w velocity components subtracted their mean value shown as vectors and the normalized magnitude of streamwise vorticity shown as colours at x/c=0.16.

Since only one set of VGs has been modelled near the centre of a two-chord wide blade section these computations cannot be used to examine the global effect of having a row of vortex generators as would be typical on the inner part on a real wind turbine blade.

The flow past a bump

To assess the capability of the immersed boundaries to model the flow past VGs an experiment was conducted in a low speed wind tunnel, where the Reynolds number was sufficiently low to allow the use of LES for comparison. The Reynolds number based on bump height is Re=1470. The 3-D velocity field was measured using SPIV at various planes normal to the main flow direction as sketched in Figure 39.
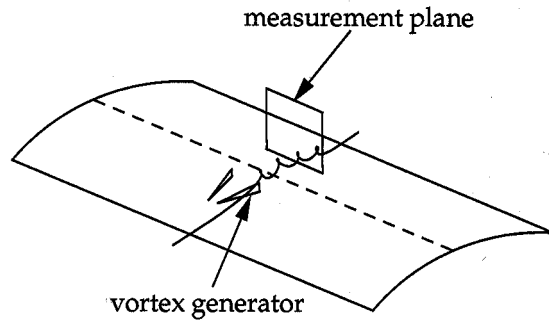

Figure 39: Sketch of location of measurement plane relative to bump and vortex generators.

The flow was also modelled using the EllipSys3D code and the immersed boundary technique to simulate the vortex generators, see Figure 40 for the computational mesh (2.7 mill cells). The computational grid was made so that the ratio between the kinematic viscosity, ν, and the turbulent viscosity ν_t, was of the order $o(1)$.
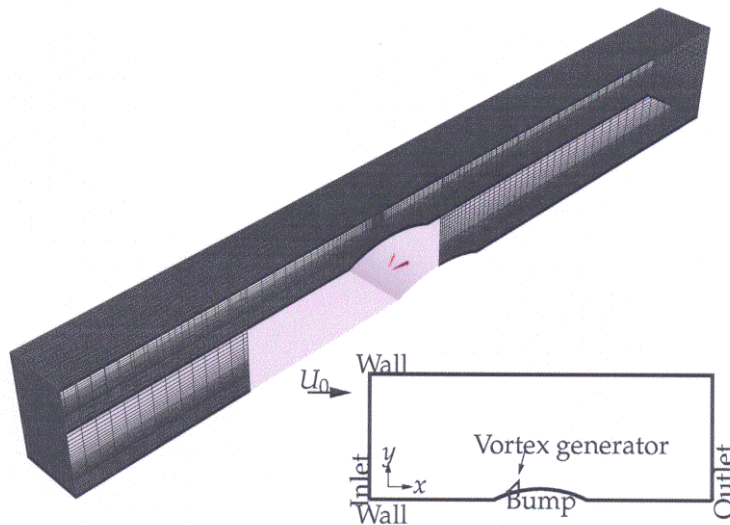
Figure 40: Computational mesh for flow past a bump on a wall.

The bump starts at x=1 m and ends at x=1.3 m and the maximum height of the bump is 3 cm. The leading edge of the two vortex generators begins at x=1.06 m and ends at x=1.104 m. In Figure 41 is shown the secondary flow at x=1.2 m for the computations and the experiment, respectively. It is seen that the flow agrees well with the expected vortices sketched in Figure 36.
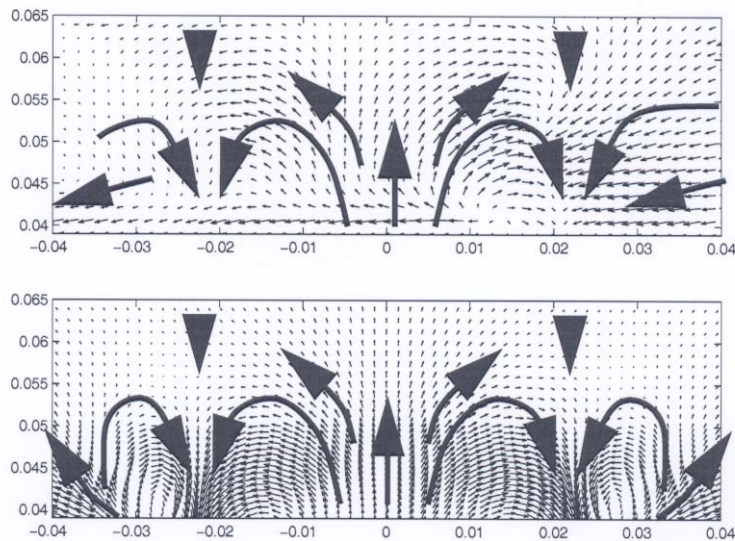
Figure 41: Secondary flow at x=1.2 m. Large arrows indicates fluid motion.
Experiments (upper), LES (lower).

In Figure 42 and Figure 43 are shown a quantitative comparison between measured and computed velocities at various locations.
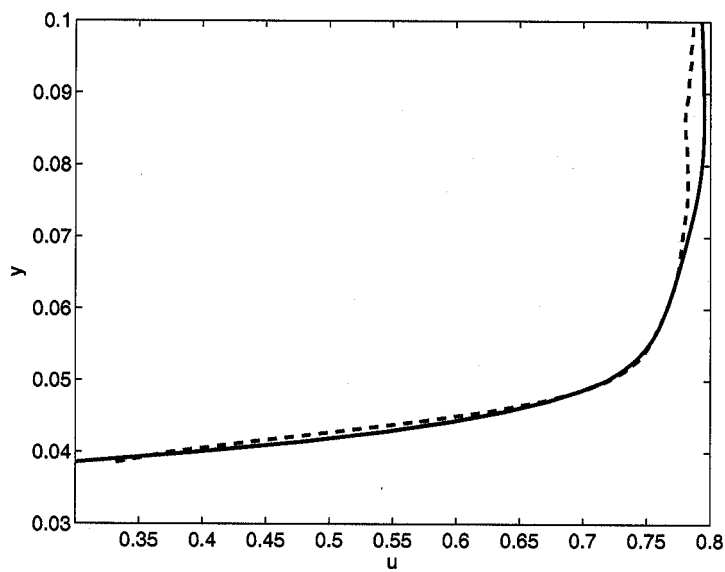

Figure 42: u velocity profile. LES (full line) and experiment (dashed). Velocity is
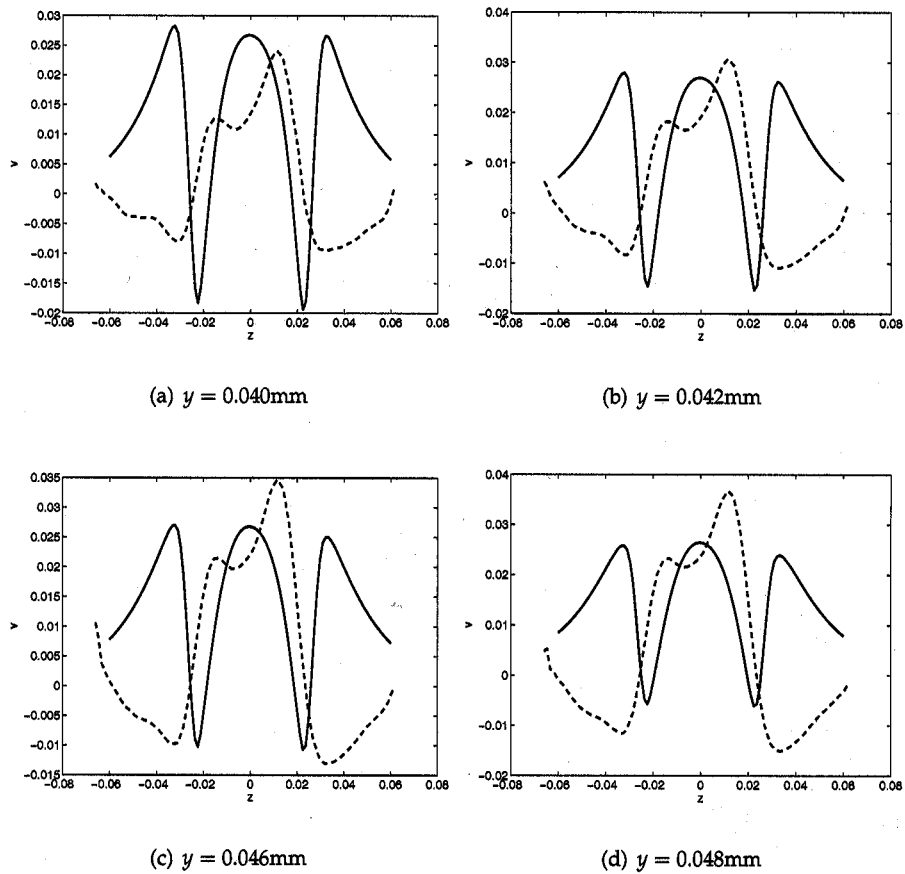*normalized with respect to inflow velocity.*

(a) $y = 0.040$mm

(b) $y = 0.042$mm

(c) $y = 0.046$mm

(d) $y = 0.048$mm

Figure 43: v velocity components at x=1.2 m at different y locations. LES (full line) and experiment (dashed line). Velocity is normalized with respect to inflow velocity.

In Figure 42 is seen that the axial velocity profile in the wind tunnel fits the experiment quite well. Figure 43 indicates a qualitative agreement of the vortices created behind the vortex generators, but the quantitative agreement shown in Figure 42 and Figure 43 is, however, not perfect.

2 Rotating 3D airfoil section with vortex generators

For the rotating blade case considered, the same airfoil section placed at a radial distance r=8m (the blade dimensions and rotational speed correspond to the LM 19m blade: Ω=2.838rad/sec) is considered. The wind velocity is U_w=12m/sec giving an incidence of 17.86°, which does not include the 3D wake effects.

NTUA contribution

In most cases, the VGs are placed at x/c=30% in different layouts (see Table 3).

Table 3: Rotating blade configuration runs, $\alpha = 17.9°$.

VGs' orientation	VGs' position (%c)	VGs' arrangement
Tip to root	30	Contra-rotating
Root to tip	10	Contra-rotating
Root to tip	30	Contra-rotating
Root to tip	30	Co-rotating

There is a significant difference between the rotating and the non-rotating case. For a rotating blade a significant radial flow is established especially within the separation bubble. Overall this effect is known as "3D-effects". Comparing the aerodynamic performance of a non-rotating with a rotating section at relatively high angles of attack, the radial flow will have a beneficial effect. The lift will increase in the rotating case as compared to the non-rotating one. This means that in the rotating case the effect of the VGs will come in addition to the effect of rotation.

As in the fixed wing case the VGs are placed at x/c=30% and two layouts are compared: the contra-rotating and the co-rotating. In the later case the VG are directing towards the tip. According to previous experience with air-jet VGs [13], there is some interest in placing co-rotating VGs looking inboard. However, in the case of air-jet VGs the mechanism is different and therefore this option was not considered at this stage for solid VGs.

Figure 44 - Figure 45 correspond to the contra-rotating case whereas Figure 46 - Figure 47 correspond to the co-rotating case.
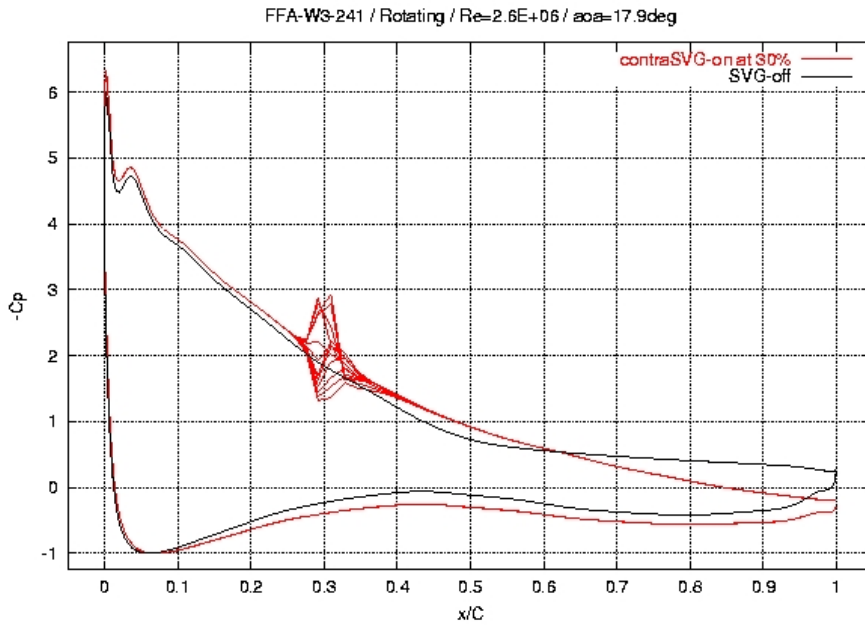
Figure 44: Predicted pressure distributions on a FFA-W3-241 rotating blade section with and without VGs at x/c= 30%, $\alpha = 18^o$ of incidence, case of contra-rotating lay-out.

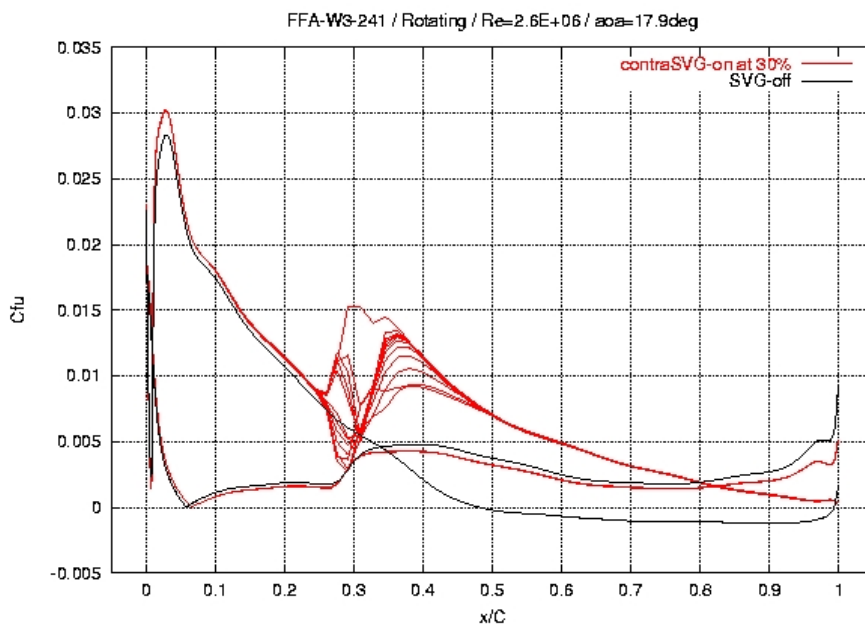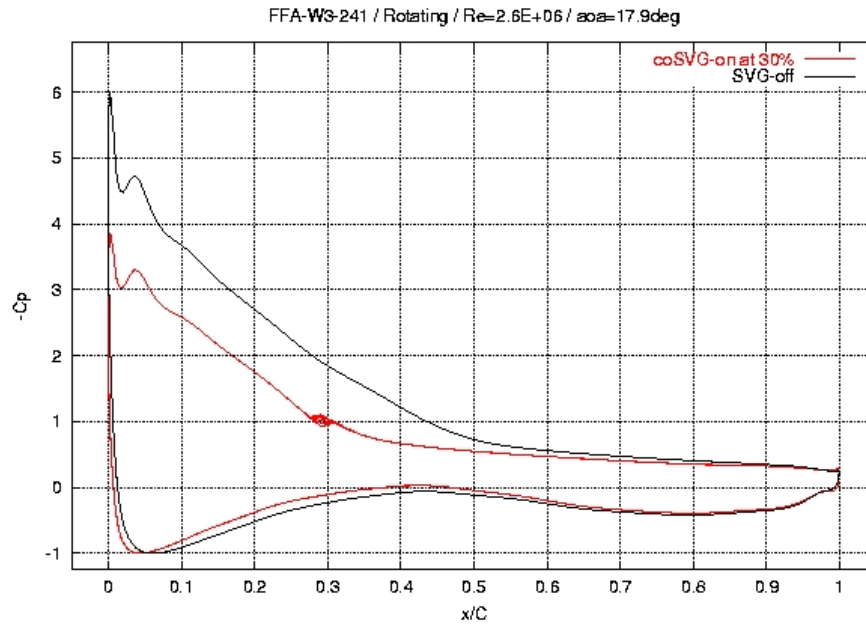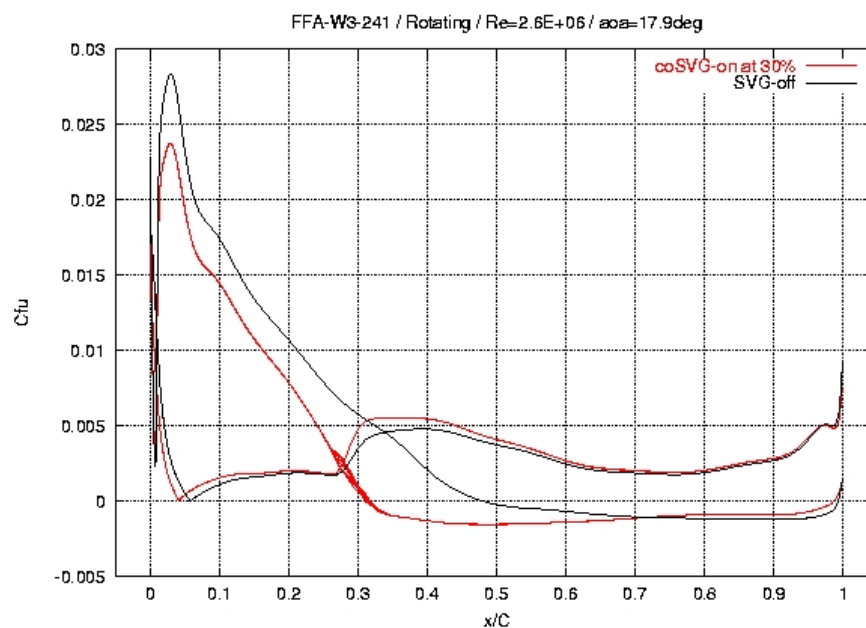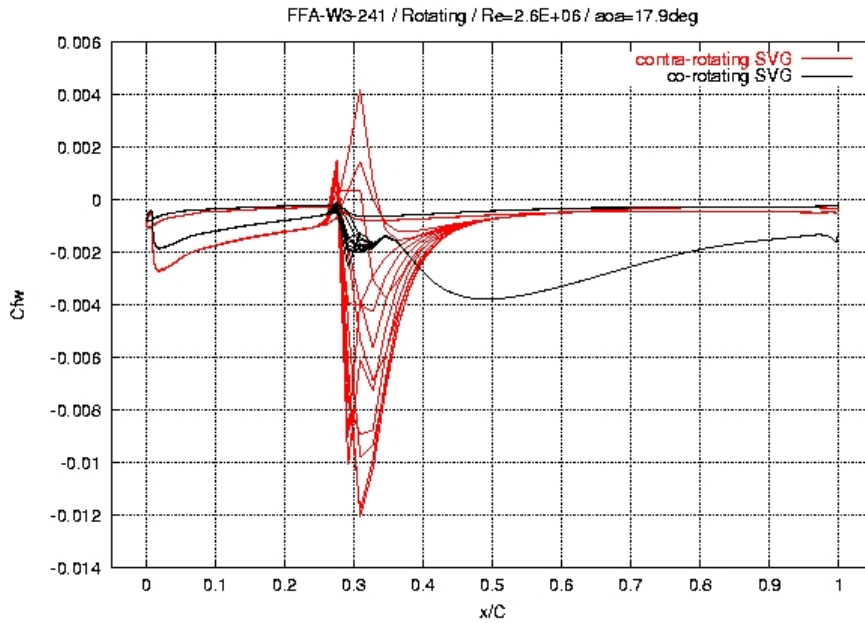*Figure 45: Predicted streamwise friction distributions on a FFA-W3-241 rotating blade section with and without VGs at x/c= 30%, $\alpha = 18^o$ of incidence, case of contra-rotating lay-out.*

Figure 46: Predicted pressure distributions on a FFA-W3-241 rotating blade section with and without VGs at x/c= 30%, $\alpha = 18^o$ of incidence, case of co-rotating lay-out.

Figure 47: Predicted streamwise friction distributions on a FFA-W3-241 rotating blade section with and without VGs at x/c= 30%, $\alpha = 18^o$ of incidence, case of co-rotating lay-out.

Figure 48: Predicted cross friction distributions on a FFA-W3-241 rotating blade section for co- and contra-rotating VGs layouts placed at x/c=30%.
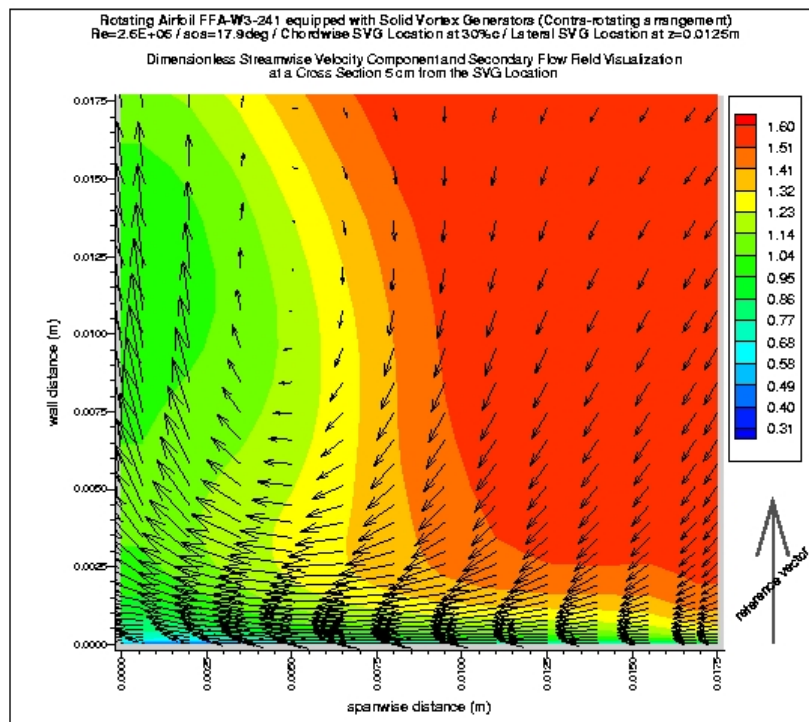
Figure 49: Cross flow vector plot and contours of the streamwise velocity component at Dx/c=5% after the VGs, case of contra-rotating lay-out on a rotating blade.
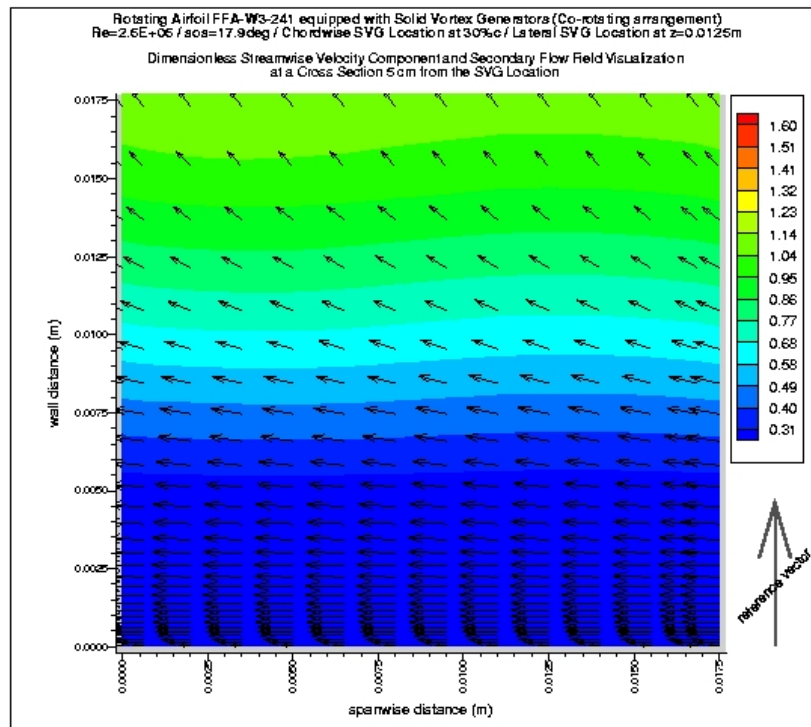
Figure 50: Cross flow vector plot and contours of the streamwise velocity component at Dx/c=5% after the VGs, case of co-rotating lay-out on a rotating blade.

In Figure 48 the cross friction distributions are compared for the two different layouts. The results are qualitatively similar to the fixed wing case.

Contra-rotating VGs will cancel separation and will increase the lift. However the increase is smaller. As already mentioned, the fact that the blade is rotating will increase the suction pressure upstream of the separation and therefore the beneficial effect of the VGs is an extra. In Figure 49, the generation of a pronounced vortex is clearly seen and so it can be concluded that the underlying mechanism is similar to the fixed wing case.

Similarly to the findings in the non-rotating case, for the co-rotating layout there is no vortex generation and therefore the effect of the VGs is negative. This is clearly seen in Figure 50 as well as in Figure 48. The contra-rotating VGs generate strong cross flow in their vicinity corresponding to a strong streamwise vortex. As a result, the cross flow in the sequel is almost completely cancelled, which explains why the effect of the VGs on rotating blades is less pronounced as compared to the fixed wing case.

Discussion

Results have been obtained on fixed and rotating blade sections equipped with solid VGs. Comparison with existing measurements shows that the mechanisms reproduced by the CFD calculations are similar to those seen in the wind tunnel tests in the fixed wing case. Quantitative comparison is also favorable. In the rotating case, a counteracting between 3D-effects and canceling of separation was found which however finally further improves the behavior of the blade.

Having concluded the development and validation of the model, it is now possible to proceed with systematic runs. Some aspects that could be investigated are:

- the dependency on some geometric parameters, such as the size and the spacing of the VGs,

- the dependency with respect to the x/c location of the VGs over a wider range of inflow conditions, in view of searching design guidelines,

- the effect on different types of airfoils.

3 Wind turbine blade with vortex generators

Only one partner has made computations on the present test case, which is a non-rotating LM 19.1 wind turbine blade equipped with one pair of VGs in a uniform flow.

VUB contribution

The Navier-Stokes used is the unstructured code FineHexa with mesh adaptation together with the mesh generator Hexpress.

It was decided to do 4 calculations with the unstructured solver: the smooth blade without rotation, the smooth blade with rotation, the blade with VG without rotation and the blade with VG with rotation. Presently results are available for the blade with VG on the coarse mesh before adaptation and the fine mesh after adaptation (with no rotation). The Smooth blade test case without rotation has been run with one adaptation. Unfortunately, the test cases with rotation were not finalized in time for publication.

	Smooth blade	Blade with VG
No Rotation	**X**	**X**
Rotation	n.a.	n.a.

Table 4: Overview of the different test cases (X= results available)

Test case 1: LM19.1 no VG and no rotation

The steady state calculation was done on a standard LM19.1 blade without rotation. The wind speed was 12 m/s and the tangential velocity was put equal to the rotational velocity at 8.5m = 24.1222 m/s. A mesh of 426953 cells was constructed using the software package Hexpress. Figure 51 shows the mesh.
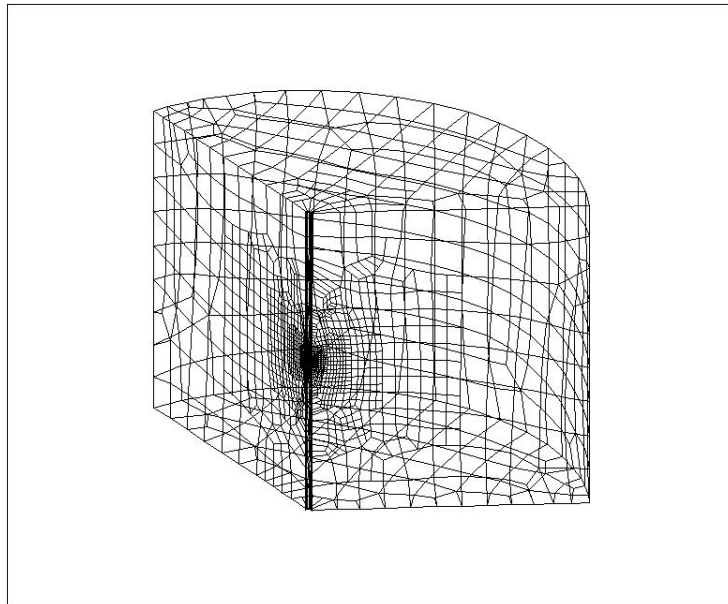
Figure 51: Mesh for test case 1

At the boundaries of the computational domain, far field boundary conditions were imposed. A second order central scheme was used at a CFL number of 2.

Preconditioning was switched on and a full multi grid strategy on 3 grids was applied. The calculation was done with the Spalart-Allmaras turbulence model .

The solution was converged to a residual drop of –2.5 before applying a mesh adaptation. The mesh adaptation includes coarsening and refining. After the adaptation the mesh contained 784617 cells and the calculation was further converged till a residual drop of –3.
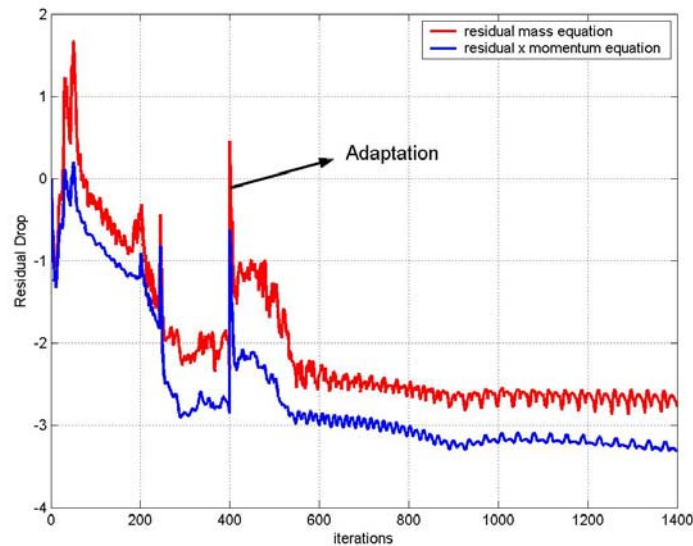

Figure 52: Residual drop test case 1

Test case 2: LM19.1 with VG without rotation

The second test case is the LM19.1 blade equipped with one pair of VGs at a radius r = 8.5m. The VGs are the same as the Delft VGs (4mm) and are scaled with the chord of the blade at 8.5m. The height of the VGs is 9.4 mm and the length 28.3 mm. The angles from the chord wise direction are 19.5°. The space between the two VGs is 18.84 mm and they are placed at 10 percent of the chord length from the leading edge.

The steady state calculation was done without rotation. The wind speed was 12 m/s and the tangential velocity was put equal to the rotational velocity at 8.5m = 24.1222 m/s.

The meshing was rather cumbersome due to big differences in length scales present in the geometry. However it was possible using Hexpress to make a rather coarse mesh of 530804 cells.

Figure 53, Figure 55 and Figure 56 show the mesh of the domain, the wing and the VGs on the coarse mesh (before adaptation). Figure 54 and Figure 57 shows the mesh after adaptation. It is seen that the adaptation performs well around the VGs; the mesh refines and tracks the vortex sheets.
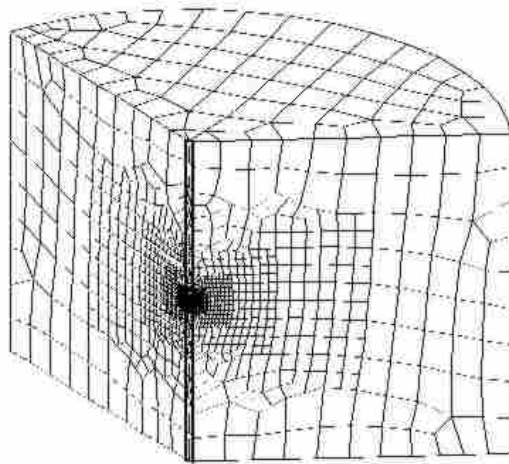
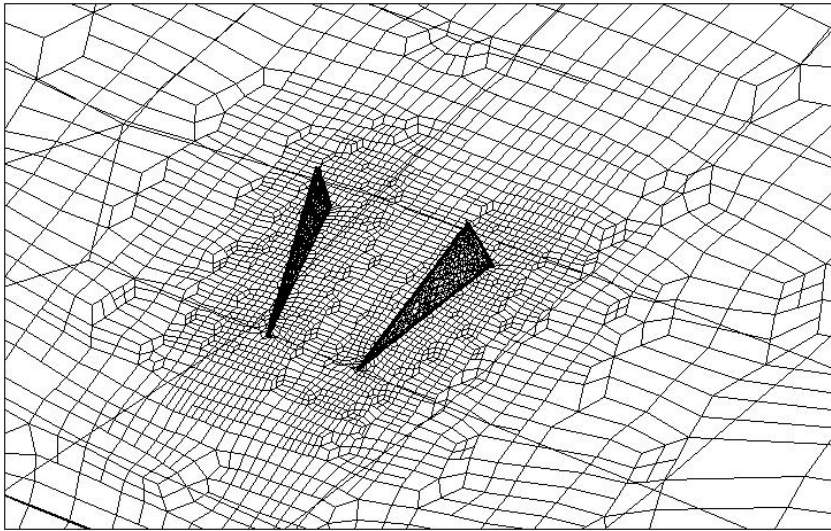*Figure 53: Computational domain with 530804 cells (coarse mesh)*
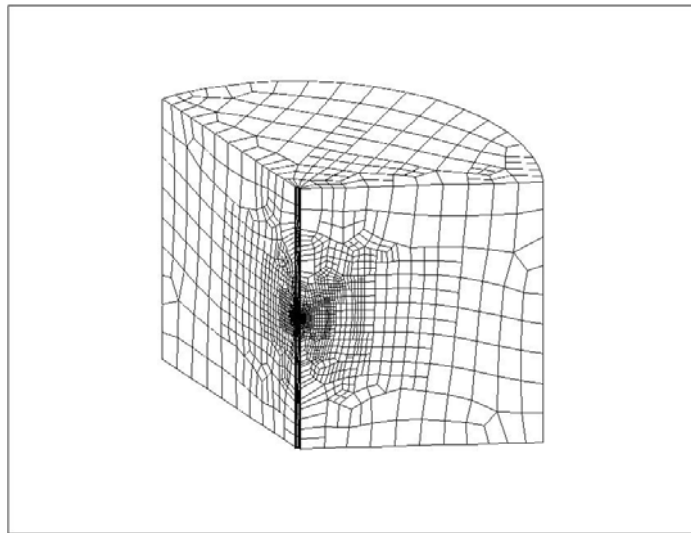
Figure 54: Computational domain after adaptation with 784617 cells (fine mesh)
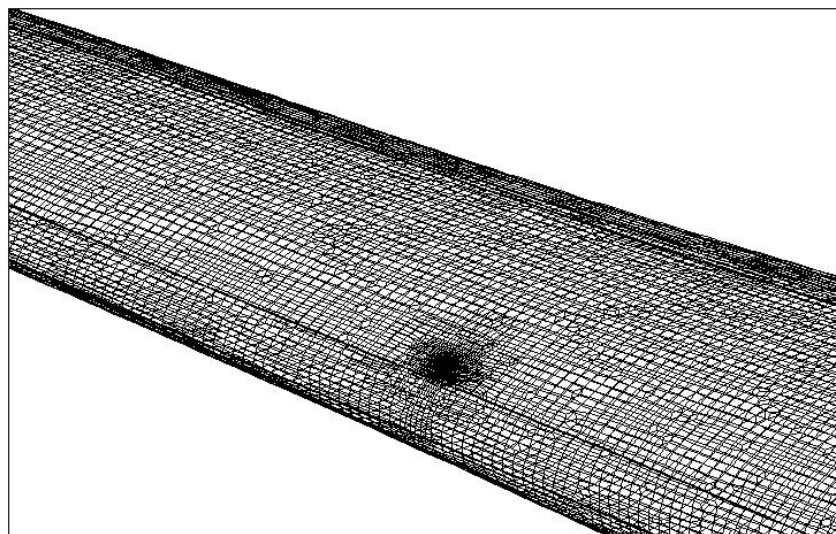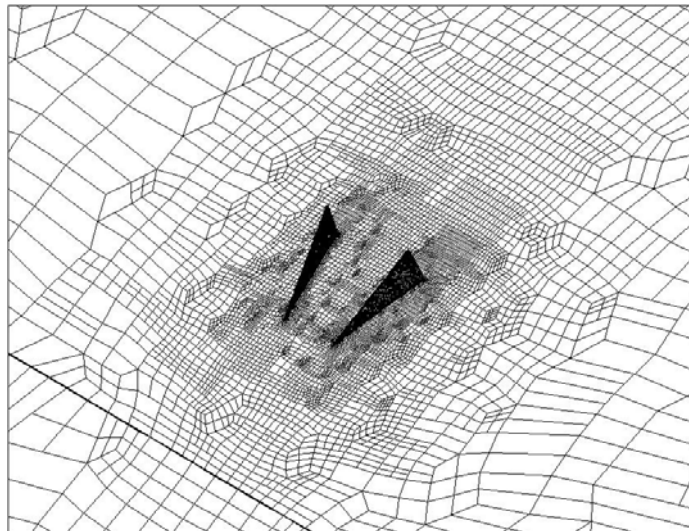

Figure 55: Close up of the mesh near the wing (coarse mesh)

Figure 56: Close up of the mesh near the VG (coarse mesh)

Figure 57: Close up of the mesh near the VG (fine mesh)

At the boundaries of the computational domain, far field boundary conditions were imposed. A second order central scheme was used at a CFL number of 2. Preconditioning was switched on and a full multi grid strategy on 3 grids was applied. The calculation was done with the Spalart-Allmaras turbulence model.

The solution was converged to a residual drop of −3.5 before applying a mesh adaptation. The mesh adaptation includes coarsening and refining. After the adaptation the calculation converged to a residual drop of −3.1
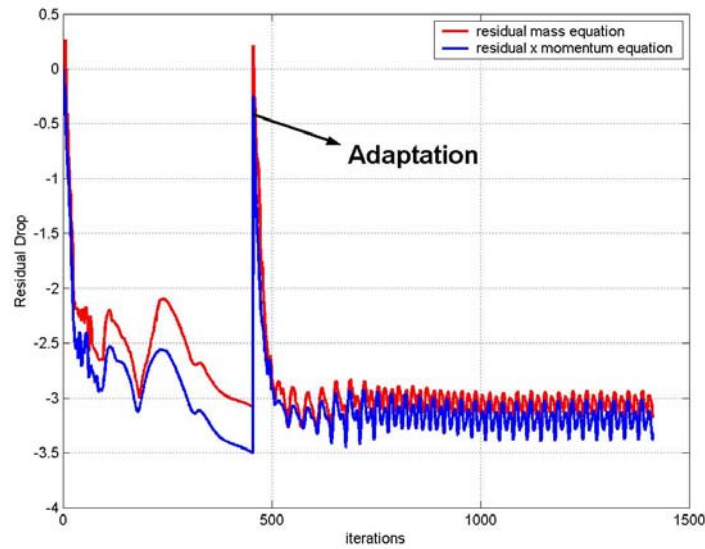
Figure 58: Residual drop for the LM19 blade with VG

Results

Test case 1

This test case was run as a reference to compare later the calculation with the VGs. Figure 59 shows the streamlines and turbulent viscosity at a cutting plane at radius =8.5 m. This is the radius at which the VG pair is placed in the second calculation. No separation takes place.
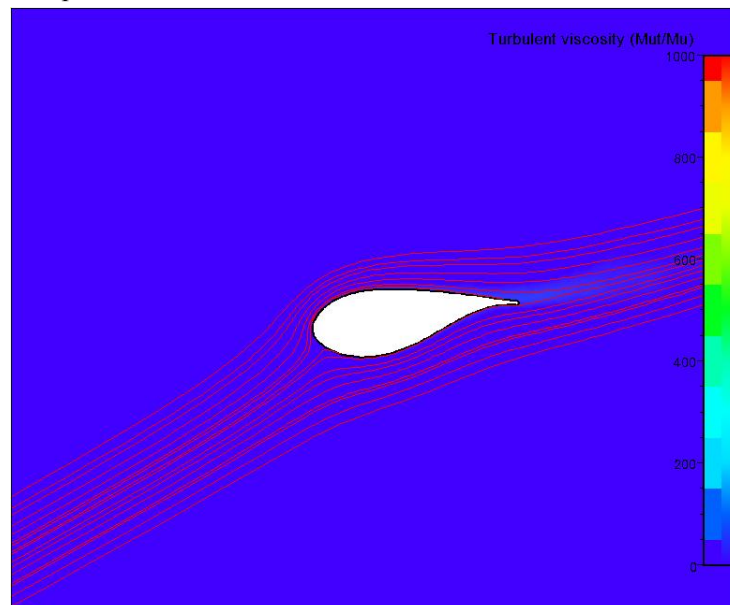
Figure 59: Streamlines and turbulent viscosity test case 1

Figure 60 shows the pressure coefficient at 3 locations with r=8.4, 8.5 and 8.6 m, while Figure 61 shows the skin friction at the same locations. There are almost no noticeable differences seen on the 3 locations.
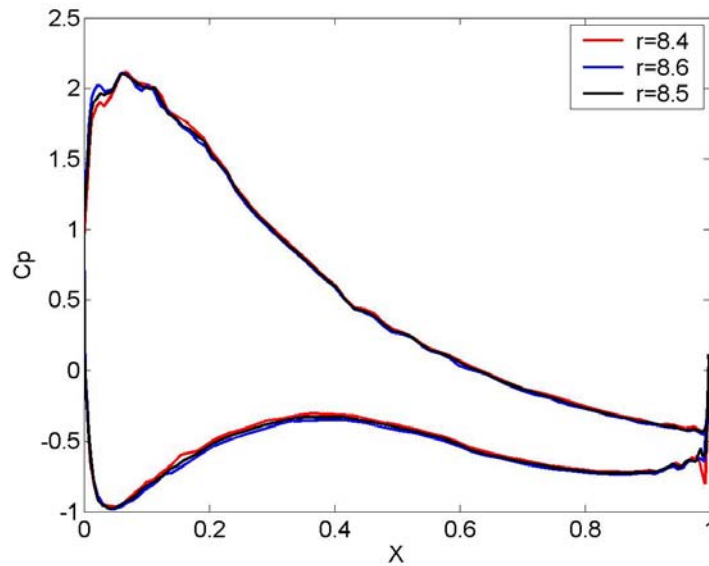
Figure 60: Pressure Coefficient at r=8.4 m, 8.5 m and 8.6 m
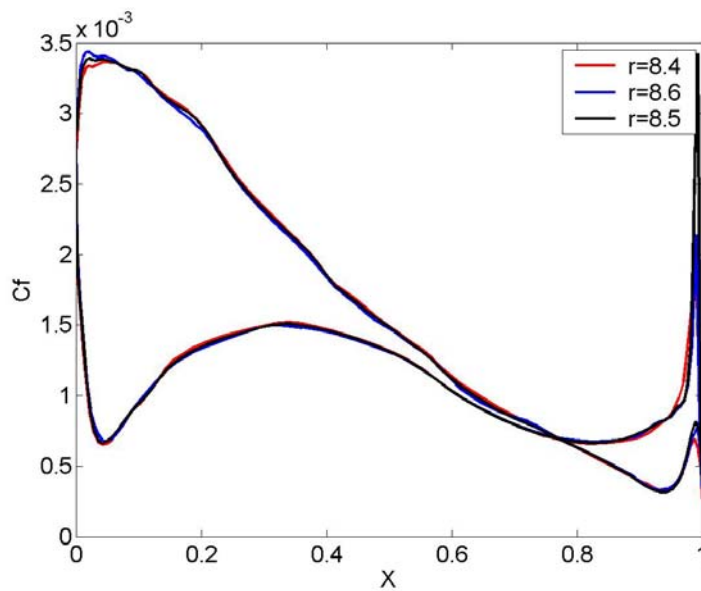
Figure 61: Skin Friction at r=8.4 m, 8.5 m and 8.6 m

Test case 2

The calculation was run until a residual drop of –3.5 was obtained before doing a mesh adaptation. This, to ensure that all flow phenomena are captured well. Figure 62 shows the locations of the 3 cutting planes where the results are shown.
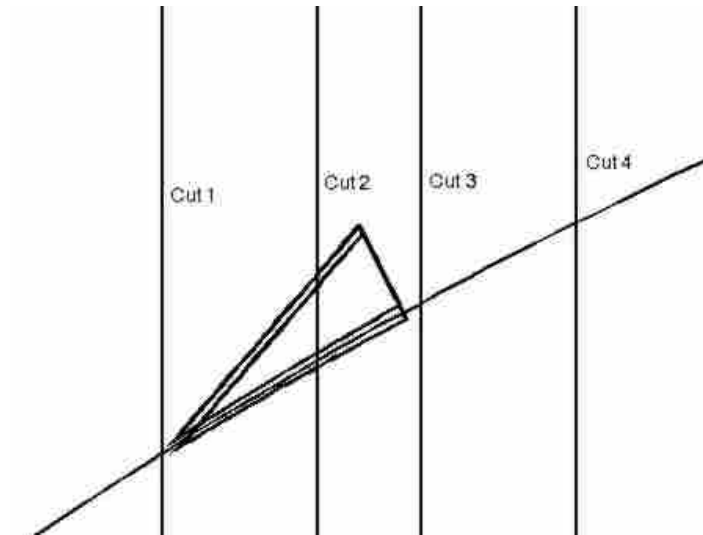
Figure 62: Locations of the 3 cutting planes

Figure 63, Figure 64, Figure 65 and Figure 66 show the magnitude of the vorticity at the 4 different cutting planes on the coarse mesh, respectively. Two vortex sheets are observed at cutting plane 2 and 3. At cutting plane 4 the vortex sheets are not visible anymore. This is because the mesh is too coarse at this region to capture the vortex sheet.
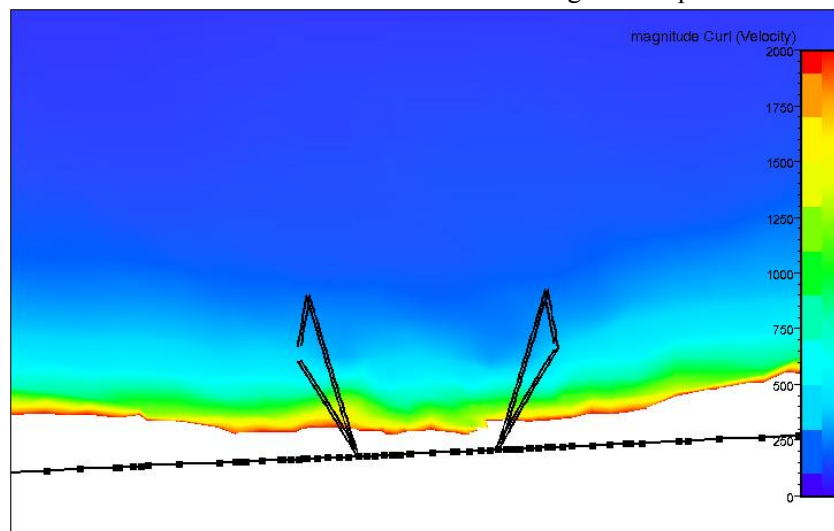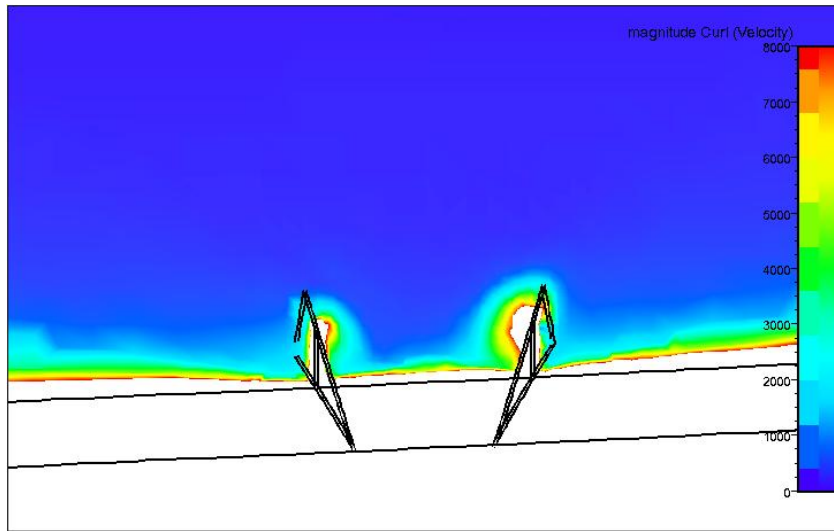

Figure 63: Vorticity at Cut 1 (coarse mesh)

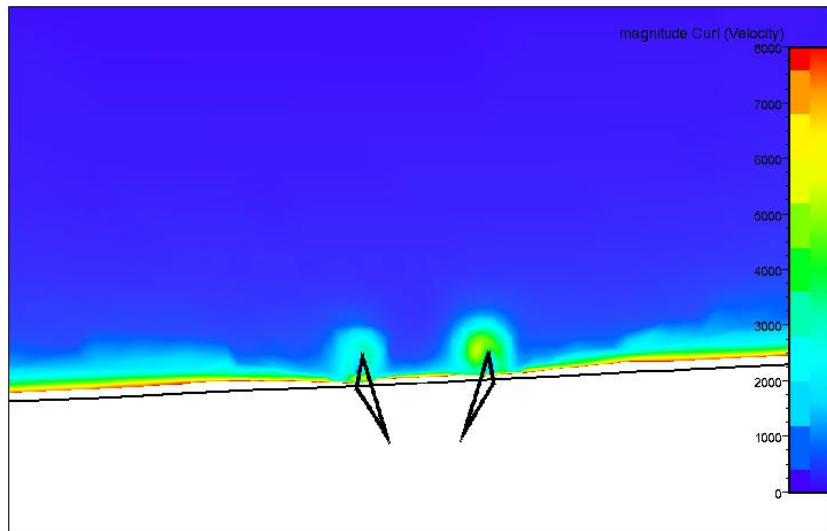*Figure 64: Vorticity at Cut 2 (coarse mesh)*

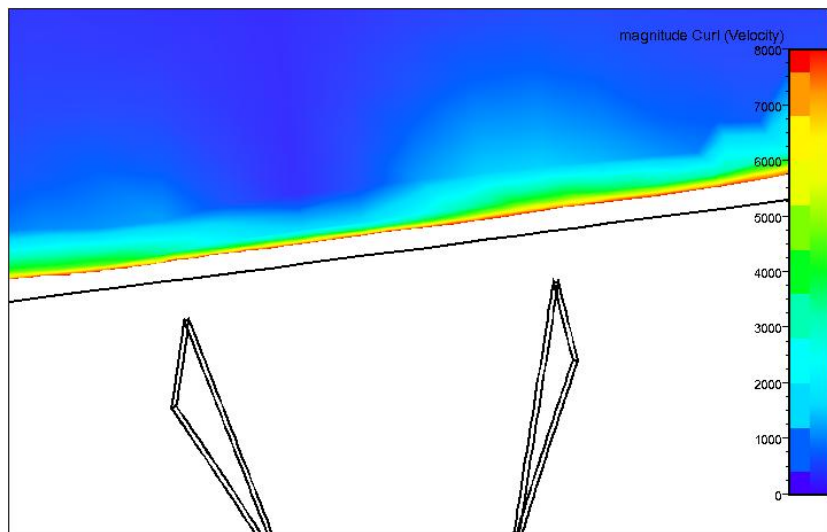*Figure 65: Vorticity at Cut 3 (coarse mesh)*

Figure 66: Vorticity at Cut 4 (coarse mesh)

Figure 67, Figure 68, Figure 69 and Figure 70 show the magnitude of the vorticity at the 4 different cutting planes on the fine mesh. Again, two vortex sheets are observed at cutting plane 1, 2, 3 and 4. Comparing these figures to the figures of the coarse mesh (Figure 63 - Figure 66) it is seen that the adaptation enhances the capturing of the vortex sheets generated by the VGs.
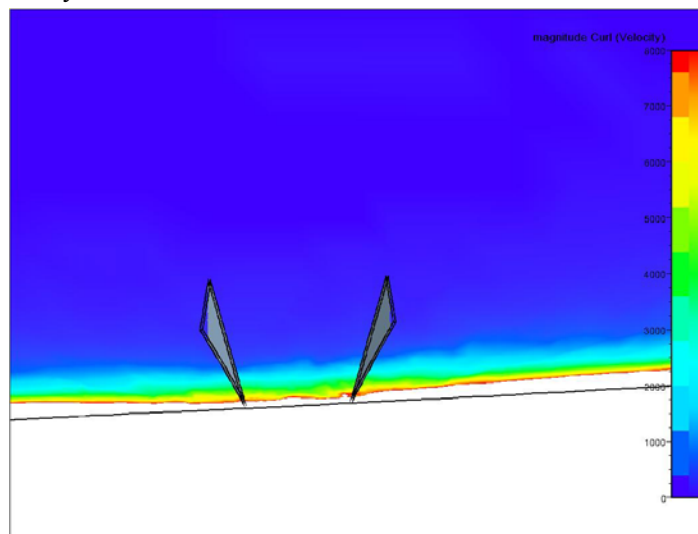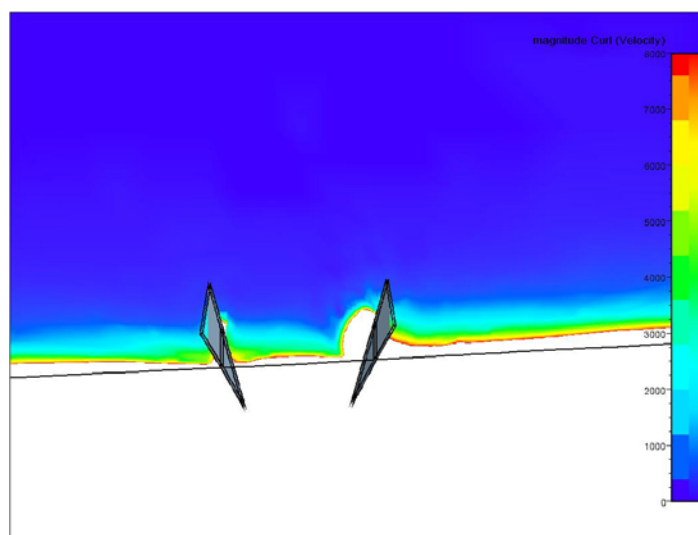

Figure 67: Vorticity at Cut 1 (fine mesh)

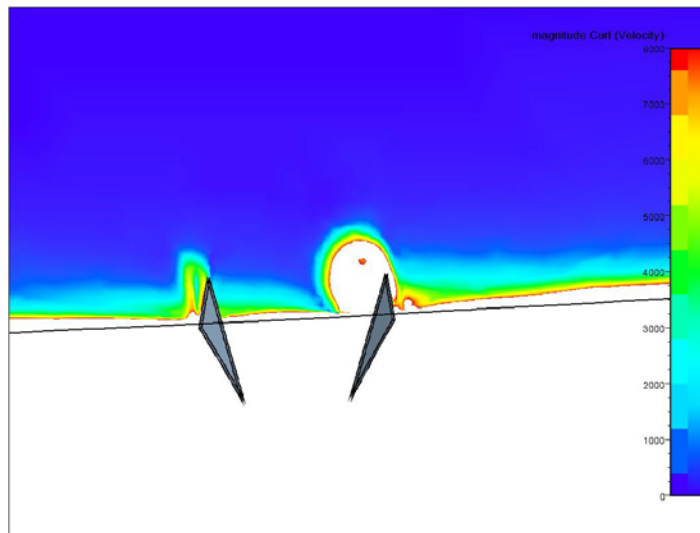*Figure 68: Vorticity at Cut 2 (fine mesh)*
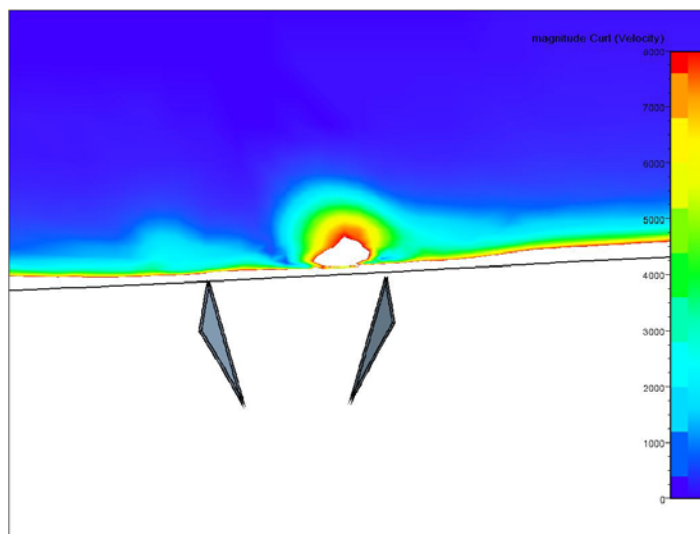
Figure 69: Vorticity at Cut 3 (fine mesh)

Figure 70: Vorticity at Cut 4 (fine mesh)

Figure 71 shows the iso-surface of the magnitude of the vorticity at a value of 1500 on the coarse mesh. The two vortex sheets are captured. However, they tend to be too short due to the coarse mesh. Figure 72 shows the same iso-surface on the fine mesh. It is seen that the vortex sheet is better captured and extends further downstream than on the coarse mesh calculation. The right VG produces a bigger vortex sheet than the left one.
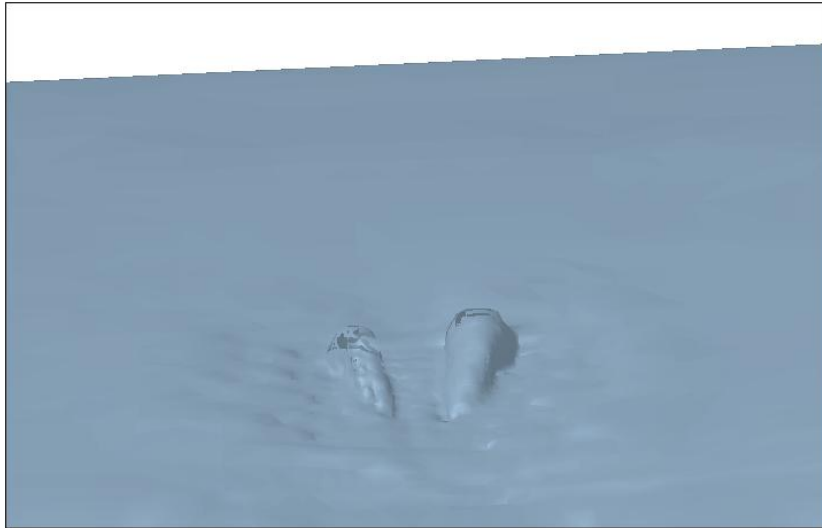
Figure 71: Iso surface of the vorticity at value 1500 (coarse mesh)
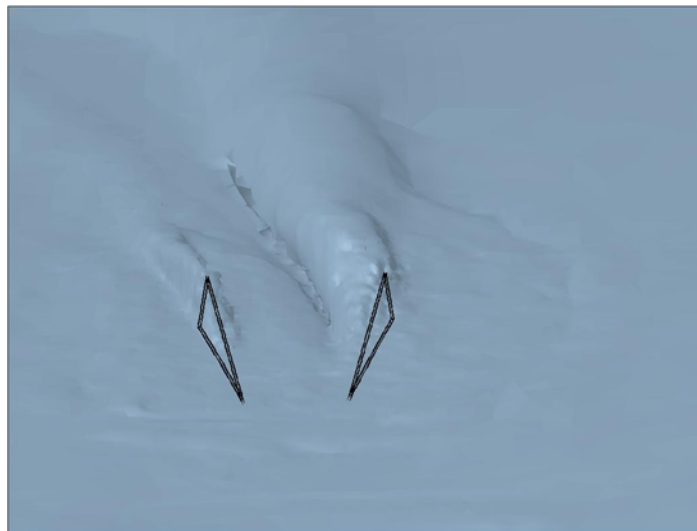
Figure 72: Iso surface of the vorticity at value 1500 (fine mesh)

The streamlines are shown at a radius of 8.5m together with the turbulent viscosity in Figure 73 for the coarse mesh. Near the trailing edge recirculation occurs. At this moment it is not clear whether the VGs delay the separation. A calculation of the smooth blade needs to be done first to be able to make a quantitative comparison. Figure 74 shows the streamlines and turbulent viscosity on the fine mesh. Separation seems to occur earlier on the fine mesh then on the coarse mesh. On the fine mesh two recirculation zones are detected.
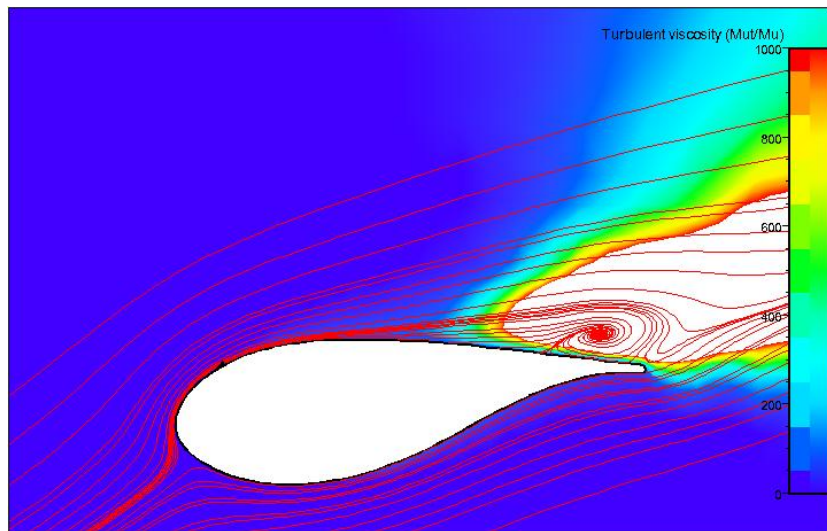
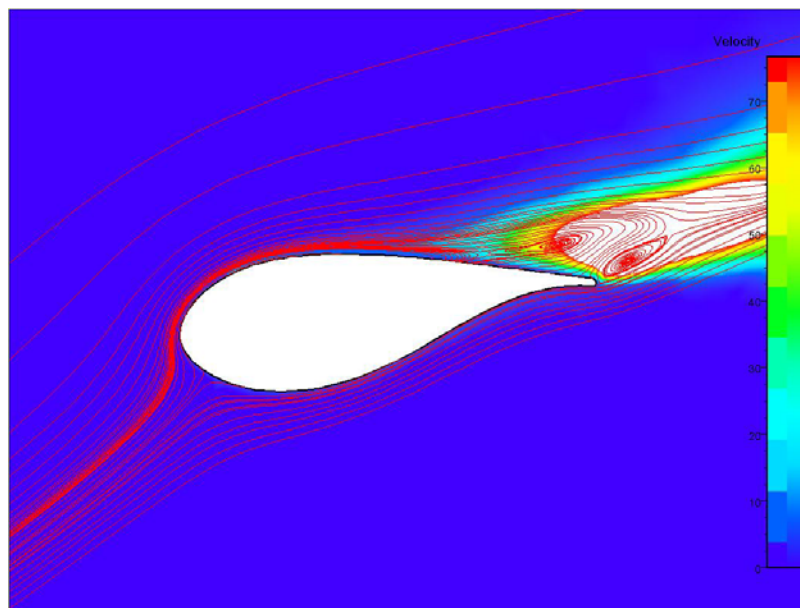*Figure 73: Streamlines and Turbulent viscosity at r=8.5m (coarse mesh)*

Figure 74: Streamlines and Turbulent viscosity at r=8.5m (fine mesh)

Figure 75 and Figure 76 show the velocity vectors at cutting plane 3 just behind the VGs for the coarse and fine mesh, respectively. The fine mesh shows a cross flow circulation, which is not captured on the coarse mesh.
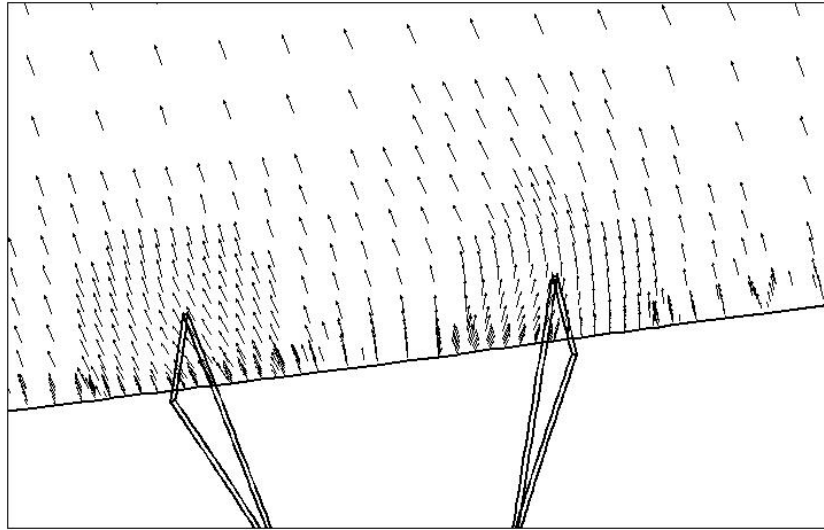
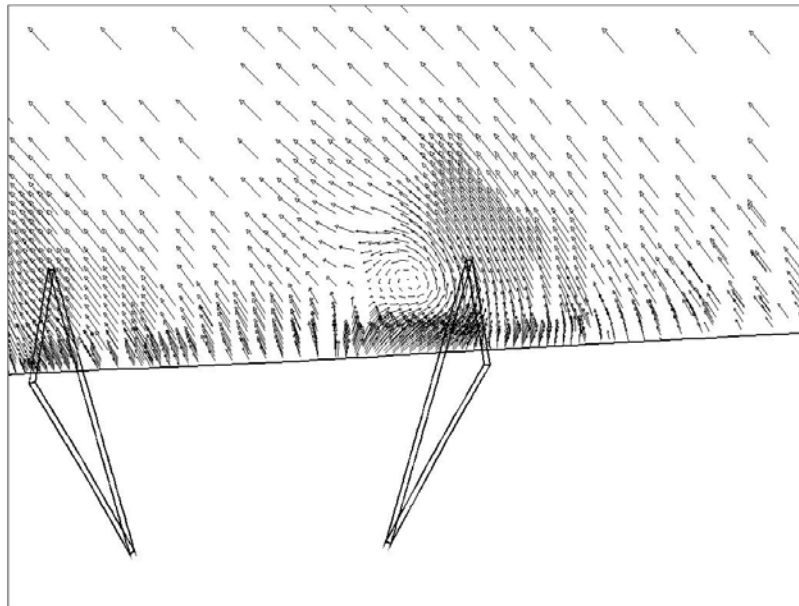*Figure 75: Velocity vectors at Cut 3 (coarse mesh)*

Figure 76: Velocity vectors at Cut 3 (fine mesh)

Figure 77 shows the skin friction coefficient around the VGs on the coarse mesh, while Figure 78 shows it for the fine mesh. It is clear that the presence of the VGs increases the skin friction tremendously. The finer mesh shows higher values for the skin friction around the VGs.
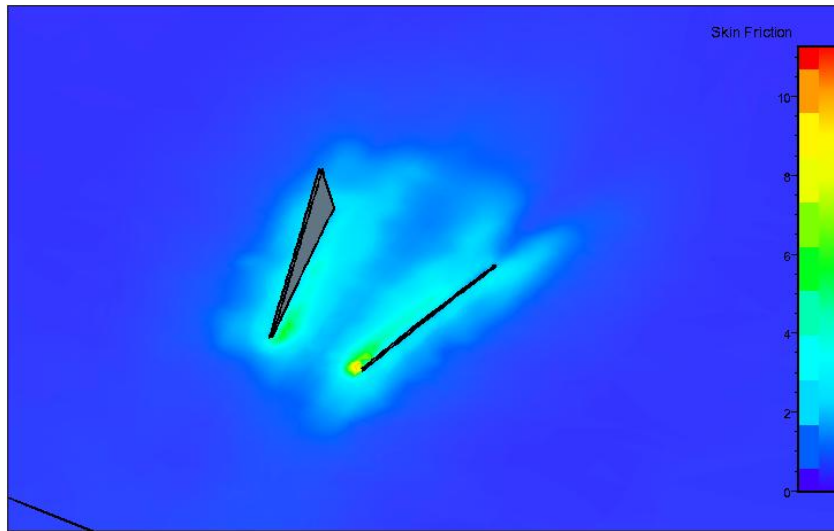
Figure 77: Skin Friction at the VG (coarse mesh)

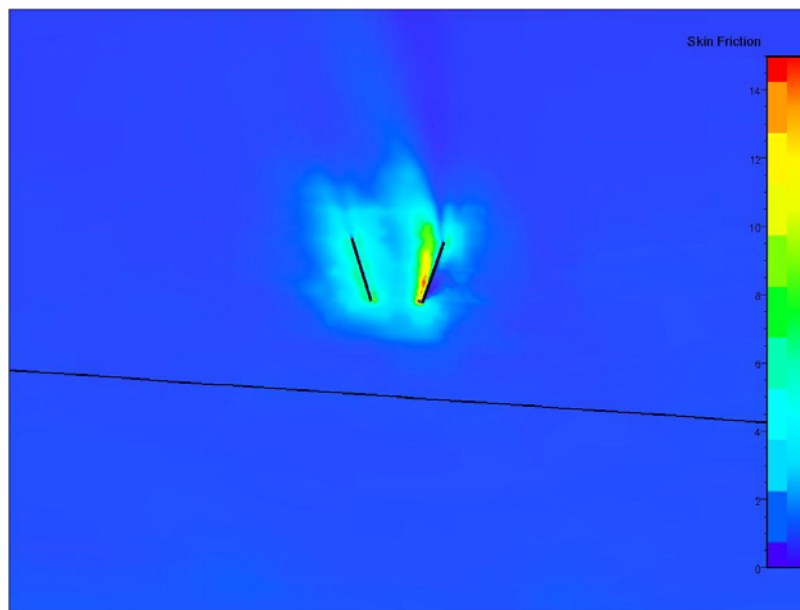*Figure 78: Skin Friction at the VG (fine mesh)*

The pressure coefficient is shown in Figure 79 and the skin friction in Figure 80 for a radius of r=8.4 m(before the VG), r=8.5 m (between the VG) and for r=8.6 m (after the VG). At 10 percent from the trailing edge a disturbance of the pressure coefficient and a tremendous increase in the skin friction is observed, indicating the presence of the VGs.
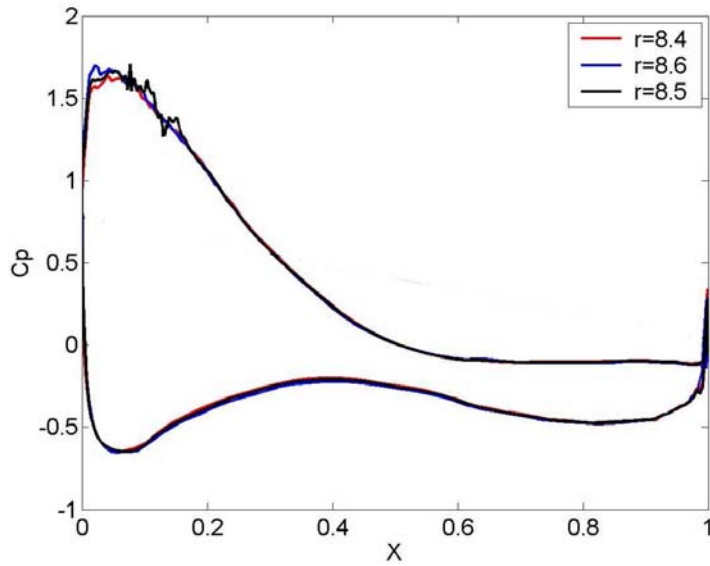
Figure 79: Cp before, between and after the VG

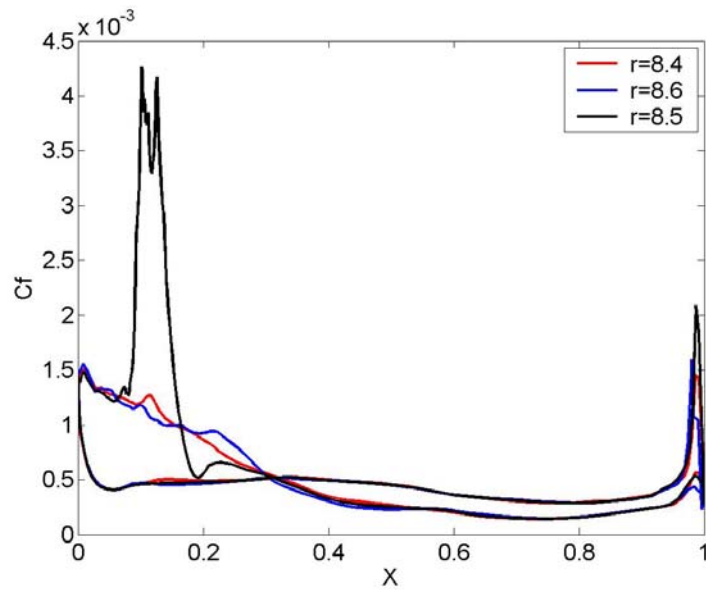*Figure 80: Cf before, between and after the VG*

A comparison of the pressure coefficient and the skin friction on the coarse and the fine mesh for r=8.5 m (between the VGs) is shown in Figure 81 and Figure 82. The pressure coefficient on the finer mesh shows less disturbances from the VG. For the skin friction the peak at the location of the VG is increasing when the mesh is refined.
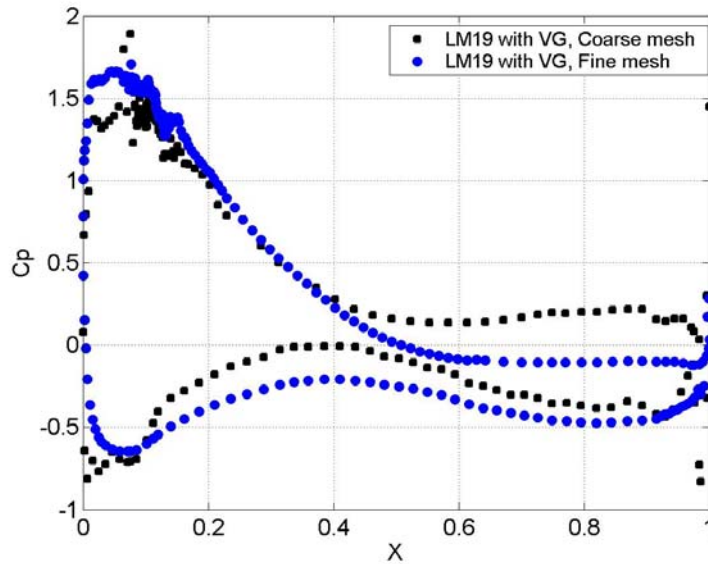
Figure 81: Cp at r=8.5m
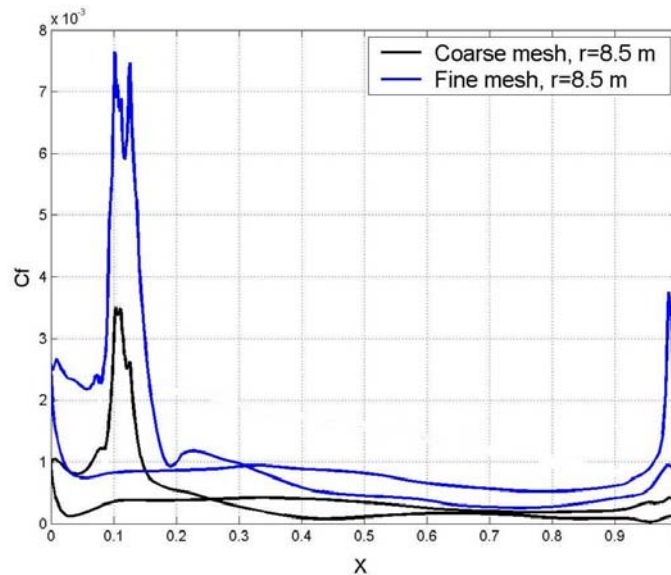
Figure 82: Skin friction at r=8.5m

A comparison of the pressure coefficient of the calculation of the standard blade without VGs (test case 1) and the calculation with VGs (test case 2) is shown in Figure 83. The pressure coefficient is overall higher for the calculation without VG. Also the difference in pressure between suction side and pressure side is bigger when there are no VG present.

Figure 84 shows the same comparison for the skin friction. It is seen that in case of VG that the skin friction is generally reduced except at the location of the VG.
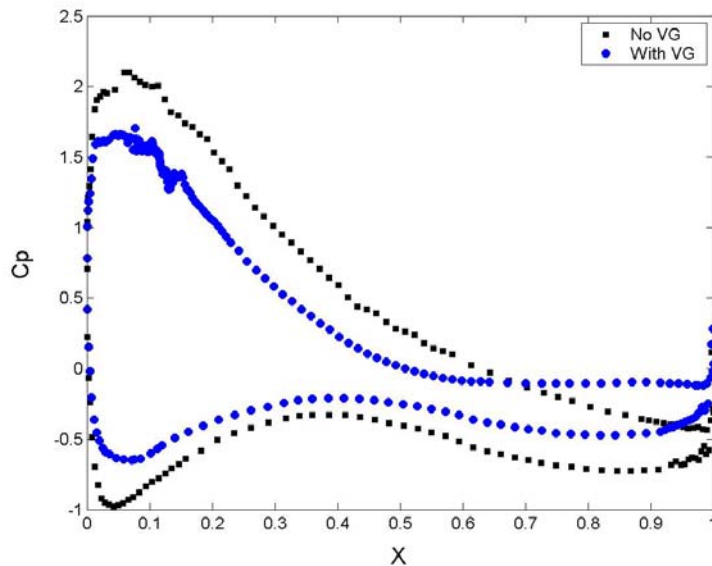
Figure 83: Pressure coefficient with VG and without VG
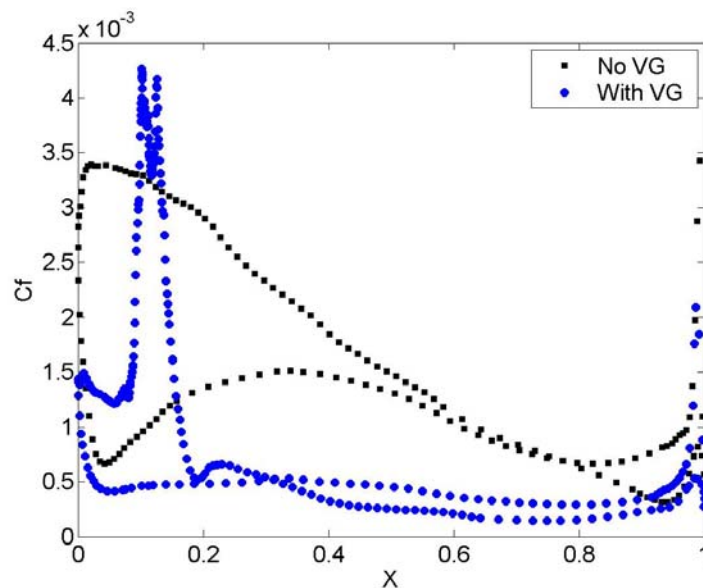
Figure 84: Skin friction with VG and without VG

Discussion

Lots of time has been spent in trying to import the plot3D format of the LM19.1 blade into the software Hexpress. This because a CAD file format is needed for the mesh generator. A coarse mesh of 530804 cells was constructed for the LM19.1 blade with VGs and a calculation on this mesh was done without rotation. After adaptation the mesh contained 784617 cells. The results of the calculation were compared between the coarse mesh and the fine mesh after adaptation. The results showed clearly the formation of two vortex sheets. The adapted mesh showed longer vortex sheets, indicating that the refinement managed to capture the flow effects.

Another calculation was done on the LM19.1 blade without VGs. This allowed seeing the influence of the VG. The VG seemed to induce separation and thus lower the skin

friction. Also the difference in pressure between suction and pressure side of the blade seemed to be lower when VGs are present. The calculations with rotation were not done since problems of convergence could not be solved.

4 Conclusions

The present report describes the work done in work package WP3.3: Aerodynamic Accessories in 3D in the EC project KNOW-BLADE. Vortex generators (VGs) are modelled in 3D Navier-Stokes solvers and applied on the flow around a 3D airfoil section and a wind turbine blade. Three test cases have been investigated. They are:

- A non-rotating airfoil section with VGs

- A rotating airfoil section with VGs

- A non-rotating wind turbine blade with VGs

The airfoil section was the FFA-W3-241 airfoil, which has been measured in the VELUX wind tunnel with and without VGs placed at different chordwise positions. Three of the partners have modelled the airfoil section as a thin airfoil section with symmetry boundary conditions in the spanwise direction to simulate an array of VGs.

The wind turbine blade is an LM19.1 blade equipped with one pair of VGs placed at radius = 8.5 m.

DLR concludes that a decrease in lift coefficient is present when the VGs are placed at x/c = 0.1 as is also seen in the measurements. Unfortunately the clean airfoil does not separate very much at high angles of attack and therefore the VGs do not delay separation as intended.

NTUA have simulated both contra-rotating and co-rotating VGs placed at several chordwise positions. Again, only a small spanwise section is modelled with symmetry boundary conditions simulating an array of VGs. Results indicate that contra-rotating VGs has the largest effect on cross flow leading to delayed stall and higher lift coefficient for a 6mm VG placed at x/c = 0.2. Also the placement of the VGs is investigated. Results indicate that placing the VGs close to the separation point has the largest effect of delaying separation.

FORTH has simulated flow over a non-rotating airfoil section with one single 4mm VG placed at x/c = 0.1 and symmetry boundary conditions in the spanwise direction. Results indicate that the VGs cause a larger separation compared to no VGs, which is in contradiction to the measurements.

DTU has modelled an airfoil section with a spanwise distance of two chord lengths and only one pair of VGs, therefore the global effect is very small. RANS, DES and LES have been used, but conclusions were that none of the methods were able to correctly predict the quantitative behaviour of the VGs. The high Reynolds number required a very large number of computational cells and therefore an alternative test case; flow over a bump at low Reynolds number, was simulated. Here both qualitative and quantitative agreement was obtained.

For the rotating airfoil section only one partner made computations, i.e. NTUA. Results indicate that an interaction between 3D effects, stemming from rotation and cancelling of separation was found, as expected. Using co-rotating VGs no vortex was generated and therefore the effect was small.

Finally, the wind turbine blade with VGs were computed by VUB and the non-rotating blade results indicated that it is possible to model the effect of a 3D VG pair resulting in

vortex sheets emanating from the VGs, but the amount of necessary computational cells is very high to make final conclusions on the effect of VGs.

In general all partners have successfully modelled vortex generators in 3D, which eventually generates vortices and mixes the boundary layer. A large effort has been on generating the numerical meshes since this is a relatively complex configuration and a large variation of length and time scales is present. Even though the quantitative agreement with measurements is not acceptable the effort spend in the present project indicate that it is possible to investigate the effect of vortex generators on wind turbine blades using 3D Navier-Stokes solvers. Much further work within independence of mesh resolution and time step as well as turbulence modelling has to be carried out in future projects before parametric variations can be investigated.

5 Acknowledgement

References

[1] Johansen et al. "KNOW-BLADE Task-2 report; Aerodynamic Accessories", Risø-R-1482(EN), Roskilde National Laboratory, Denmark, November 2004.

[2] Fuglsang P., Antoniou I., Dahl K.S., Madsen H.A. "Wind Tunnel Tests of the FFA-W3-241, FFA-W3-301 and NACA63-430 Airfoil", Risø-R-1041(EN), Risø National Laboratory, Denmark, December, 1998

[3] Brodersen, O.; Hepperle, M.; Ronzheimer, A.; Rossow, C.-C.; Schoening, B.: "The Parametric Grid Generation System MegaCads", Proc. of the 5th International Conference on Numerical Grid Generation in Comp. Field Simulation; NSF Engineering Center, MS, USA, pp. 353-362, 1996.

[4] CentaurSoft: "http://www.centaursoft.com", 2004.

[5] Kroll, N.; Rossow, C.-C.; Becker, K.; Thiele, F.: "The MEGAFLOW Project. Aerospace Science and Technology", Volume 4, 2000, pp. 223-237.

[6] Spalart, P. R. and Allmaras, S. R.: "A One-Equation for Aerodynamic Flows", AIAA Paper 92-0439, AIAA, 1992.

[7] Menter FR "Zonal Two Equation k-ω Turbulence Models for Aerodynamic Flows". AIAA-93-2906, 1993.

[8] Voutsinas, S.G., Belessis, M.A., Perivolaris, Y., Riziotis, V.A., "Wind Turbine Blades Equipped with Airjet Vortex Generators: Full Scale Verification of Blade Optimised for increased performance and manufacturing", Final Report for the DG XII-EU project, AIR-JETS BLADES, 1997-2000.

[9] Michelsen JA "Basis3D - a Platform for Development of Multiblock PDE Solvers.", Technical Report AFM 92-05, Technical University of Denmark, 1992.

[10] Michelsen JA "Block structured Multigrid solution of 2D and 3D elliptic PDE's." Technical Report AFM 94-06, Technical University of Denmark, 1994.

[11] Sørensen NN "General Purpose Flow Solver Applied to Flow over Hills." Risø-R-827-(EN), Risø National Laboratory, Roskilde, Denmark, June 1995.

[12] Mads Reck, "Computational fluid dynamics, with detached eddy simulation and immersed boundary technique, applied to oscillating airfoils and vortex generators", Ph.D. thesis at MEK/DTU to appear 2004.

[13] Bender, E.E., Anderson, B.H., Yagle, P.J., "Vortex Generator Modeling for Navier-Stokes Codes", FEDSSM99-6919, 3rd Joint ASME/JSME Fluids Engineering Conference, San Francisco, CA, 1999.

Mission

To promote an innovative and environmentally sustainable technological development within the areas of energy, industrial technology and bioproduction through research, innovation and advisory services.

Vision

Risø's research **shall extend the boundaries** for the understanding of nature's processes and interactions right down to the molecular nanoscale.

The results obtained shall **set new trends** for the development of sustainable technologies within the fields of energy, industrial technology and biotechnology.

The efforts made **shall benefit** Danish society and lead to the development of new multi-billion industries.